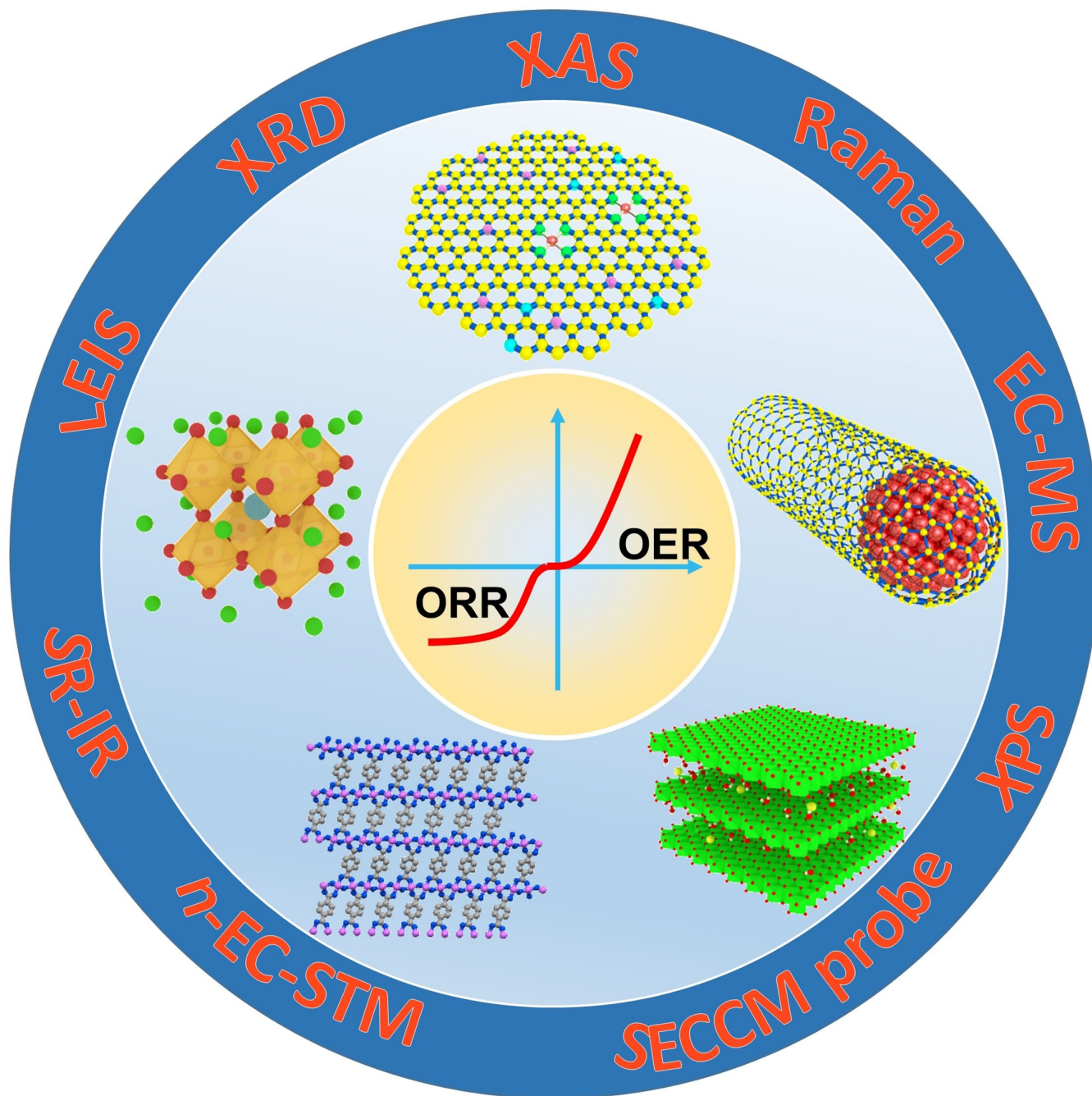


VIP Very Important Paper

Special  
Collection

# A Review on Experimental Identification of Active Sites in Model Bifunctional Electrocatalytic Systems for Oxygen Reduction and Evolution Reactions

Shujin Hou<sup>+, [a, b]</sup> Regina M. Kluge<sup>+, [a]</sup> Richard W. Haid<sup>+, [a]</sup> Elena L. Gubanova<sup>[a]</sup>  
Sebastian A. Watzele<sup>[a]</sup> Aliaksandr S. Bandarenka<sup>\*, [a, b]</sup> and Batyr Garlyyev<sup>\*, [a]</sup>



Efficient electrocatalysis of the oxygen reduction (ORR) and evolution (OER) reactions is essential in numerous renewable energy conversion systems, such as fuel cells, metal-air batteries, and water electrolyzers. Design and optimization of electrocatalytic materials for such systems primarily rely on understanding the nature of active centers on the catalyst surface. This review focuses on several important aspects of the

experimental identification of active sites on various model bifunctional ORR/OER electrocatalytic surfaces. Applications of the state-of-the-art experimental techniques are analyzed. In addition, approaches to investigate and understand the influence of some supporting electrolyte components on the ORR and OER activities are discussed.

## 1. Introduction

The performance of numerous renewable energy conversion systems is governed by the electrocatalytic activity of the involved catalyst materials. Especially, the efficient electrocatalysis of the oxygen reduction (ORR) and oxygen evolution reactions (OER) is crucial for several energy conversion systems such as water electrolyzers, fuel cells, and metal-air batteries. As introduced by Taylor in 1925, the rate of the catalytic reactions is controlled by several highly active centers on the surface.<sup>[1]</sup> Hence, the identification of such active sites is paramount in optimizing the performance of the catalyst. In the past decade, there has been an increasing amount of research focusing on the precise determination of the active centers on electrocatalytic surfaces. Table 1 presents an overview of several state-of-the-art bifunctional ORR/OER materials. The table also provides information about the location of active centers and the techniques used in their identification.

In general, the reaction mechanisms of the OER and ORR depend on the type of electrolyte (acidic or alkaline media).<sup>[2–5]</sup> The ORR can proceed either through a direct four-electron or a two consecutive two-electron transfer,<sup>[6]</sup> whereas the OER mostly follows the four-electron transfer mechanism.<sup>[2,5]</sup> Both reactions include oxygen-comprised intermediates such as \*O, \*OH, \*OOH. Nørskov *et al.* proposed so-called “volcano plots” for the OER and ORR, where the calculated Gibbs free energies were presented for each elementary step as a function of binding energy of oxygen-comprised intermediates.<sup>[2]</sup> Calculations were performed for metal and metal oxides surfaces. It was shown that the limiting steps for the OER are the \*OOH and the \*O formation, while for the ORR they are the \*OH and O<sub>2</sub> reduction.<sup>[2,7]</sup> These findings highlight that the binding energies of intermediates for the most efficient OER and ORR

catalysts are different. However, an optimization of the morphological, topological, and electrical properties of the catalyst can assist in achieving an optimal catalyst with bifunctional activity.

This review consists of six sections, with the main emphasis on the experimental studies on the ORR and OER catalysts. The review starts with extended surfaces, such as single crystalline and thin-film materials, where metal- and non-metal-based electrocatalysts are considered. Afterward, the focus is set on the recent developments of metal-organic framework (MOF) derived catalysts materials. Later, structure-activity relations are elaborated using the examples of size- and mass-selected nanoparticles. Then, the influence of certain components present in the supporting electrolytes is discussed. Last but not least, several instrumentations used in the elucidation of active sites on the surfaces of electrocatalysts are discussed in more detail. Herein presented concepts and experimental methods are aimed to serve as a guideline in the optimization and design of bifunctional electrocatalysts.

## 2. Extended Surfaces

In order to elucidate the nature of active sites, well-defined model surfaces are needed. Such model surfaces can be metal single crystals or oxide thin films epitaxially grown, *e.g.*, by molecular beam epitaxy (MBE) or pulsed laser deposition (PLD). Studies on well-defined thin films are rare compared to powder ink films. Still, they are necessary for profound studies as they provide the exposure of well-defined crystal facets and stoichiometry. In the following, we introduce an excerpt of studies performed on extended surfaces and thin films elucidating the catalyst's active sites towards the ORR and OER. This section is divided according to popular material classes: single metals and their oxides, oxides consisting of more than one metal (*e.g.* found in perovskite structures), and carbon-based alternatives.

### 2.1. Single Metal (Oxides)

To date, noble metal catalysts such as platinum (Pt) and iridium/ruthenium (Ir/Ru)-based materials have been reported as state-of-the-art for the ORR and OER, respectively. Studies on well-defined Pt(111) surfaces revealed that the ORR active sites are located at sites with relatively high coordination, as can be found, for instance, near the bottom of step edges on extended surfaces.<sup>[23,24]</sup> Concerning the Ir/Ru oxide thin films, the

[a] S. Hou,<sup>†</sup> R. M. Kluge,<sup>†</sup> R. W. Haid,<sup>†</sup> Dr. E. L. Gubanova, Dr. S. A. Watzel, Prof. A. S. Bandarenka, Dr. B. Garlyyev  
Physics of Energy Conversion and Storage, Physik-Department  
Technische Universität München  
James-Franck-Str. 1, 85748 Garching bei München, Germany  
E-mail: bandarenka@ph.tum.de  
batyr.garlyyev@tum.de

[b] S. Hou,<sup>†</sup> Prof. A. S. Bandarenka  
Catalysis Research Center TUM  
Ernst-Otto-Fischer-Str. 1, 85748 Garching bei München, Germany

[<sup>†</sup>] These authors contributed equally to this work.

 An invited contribution to a Special Collection on Bifunctional Electrocatalysis

 © 2021 The Authors. ChemElectroChem published by Wiley-VCH GmbH. This is an open access article under the terms of the Creative Commons Attribution License, which permits use, distribution and reproduction in any medium, provided the original work is properly cited.

orientation was found to be a crucial parameter for the OER activity. Shao-Horn and co-workers investigated well-defined rutile  $\text{IrO}_2$  and  $\text{RuO}_2$  films with both (110) and (100) orientations in the alkaline environment of 0.1 M KOH.<sup>[25]</sup> Using cyclic voltammetry (CV) and galvanostatic measurements, the authors

found that the (100) surfaces outperformed their (110) counterparts. The OER activity followed the trend as  $\text{RuO}_2(100) > \text{RuO}_2(110) > \text{IrO}_2(100) > \text{IrO}_2(110)$ . The authors explained the superior performance of the (100) orientation by a higher density of active coordinatively undersaturated (cus) metal sites



Shujin Hou obtained his bachelor's degree in chemical engineering and technology from Tianjin Polytechnic University in 2015. Subsequently, he went to East China Normal University to do his master thesis under the supervision of Prof. Likun Pan and obtained his master degree in material science and optoelectronics in 2018. He is currently a PhD candidate in the Prof. Aliaksandr S. Bandarenka's group. His research interest focuses on the design and synthesis of MOFs and MOF-derived materials for enhanced electrocatalysis.



Regina M. Kluge is a PhD candidate at the chair for Energy Conversion and Storage at the Technical University of Munich. She received her Master in Condensed Matter Physics at the same university in 2017, where she was concentrating on functional materials for energy conversion, more precisely organic thermoelectric materials. Since she never lost her interest in the central topic of energy, her current research is focusing on the determination of electrocatalytically active sites via electrochemical scanning tunneling microscopy.



Richard Haid received his bachelor's and master's degree in physics at the Technical University of Munich, where he is currently a PhD student at the chair for energy conversion and storage. His research focuses on the electrochemical processes at the electrode/electrolyte interface of energy related systems. He is specialized in the application of scanning tunneling microscopy under reaction conditions for the identification of active electrocatalytic sites.



Dr. E. Gubanova studied chemical process engineering at the Tomsk Polytechnic University (Russia) and completed her jointly supervised PhD with Profs. Drs. V. A. Sadykov and C. Mirodatos in 2008 at Boreskov Institute of Catalysis (Siberian Branch of Russian Academy of Sciences), Novosibirsk, Russian Federation and IRCELYON (CNRS/Université Claude Bernard Lyon1), Villeurbanne, France. After working as a junior researcher at Boreskov Institute of catalysis, she was awarded in 2010 fellowship at Ruhr University Bochum (Germany) with Prof. Dr. M. Muhler. In 2011 she joined the group of Prof. Dr. J. Lercher at Technical University of Munich (Germany), where she is now working in the Department of Physics of Energy Conversion and Storage of Prof. Dr. A. S. Bandarenka. Her scientific interests are focused on the electrocatalysis for energy applications.



Dr. S. A. Watzele received his M.Sc. degree in physics in 2016 from Technical University of Munich (Germany), where he worked on benchmarking catalysts for water splitting reactions in the group of Energy Conversion and Storage. During his doctorate at the same chair, he focused on the characterization of electrode material and the synthesis of active nanostructured catalysts for fuel cell applications under the supervision of A. Bandarenka. He received a fellowship from the Nano-systems Initiative Munich and the International Graduate School of Science and Engineering. After receiving his PhD degree in 2020 he continued working as a postdoctoral researcher.



Aliaksandr S. Bandarenka received his PhD degree in 2005 from Belarusian State University. After a postdoc at the University of Twente, Netherlands and Technical University of Denmark, he was a group leader in the Center for Electrochemical Sciences (CES) at Ruhr University Bochum (2010–2014). Currently, he is an Associate Professor at the Department of Physics, Technical University of Munich, Germany. His research interests are focused on the development of electrocatalysts, methodologies for characterization and modification of electrified solid/liquid interfaces, and interfacial charge transfer.



Dr. B. Garlyyev received M.Sc. degree from Georgia Institute of Technology (Atlanta, USA) in 2013 and PhD degree from the same institute in 2016, where he worked on synthesis of nanostructured materials with Prof. Dr. M.A. El-Sayed. Thereafter, he started his postdoctoral research in the group of Prof. Dr. A.S. Bandarenka at Technical University of Munich (Germany) and since October of 2020 he is a group leader at the same chair. His research focuses on electrocatalysis for green energy conversion technologies. In the summer of 2016, Dr. Garlyyev was awarded TUM University Foundation Fellowship.

**Table 1.** Performances and the suggested active sites of recently reported bifunctional ORR/OER electrocatalysts, as well as the methods applied for the identification of active sites.

Catalyst	OER E [V], at j = 10 mA cm <sup>-2</sup>	ORR E <sub>onset</sub> [V]	E <sub>1/2</sub> [V]	ΔE [V] E <sub>j=10</sub> - E <sub>1/2</sub>	Active sites	Experimental method for the identification of active sites	Ref.
Co-MOF/GF	1.45	0.78	0.70	0.75	MOF derived CoOOH species	SEM, Raman spectroscopy, FT-IR, XPS, and XRD	[8]
Co <sub>3</sub> HITP <sub>2</sub>	1.59	0.91	0.80	0.79	Metal centers with unpaired 3d electrons	EPR, XPS, and EXAFS	[9]
Mn/Fe-HIB-MOF	1.51	0.98	0.88	0.63	Carbon active sites	Atomic-resolution STM, Fourier-transforms of the EXAFS spectra, and XPS	[10]
Defective Graphene	1.57	0.91	0.76	0.81	Defects at the edge pentagon	HAADF image	[11]
O-NGM-800	1.70	0.93	0.86	0.84	Oxygen-induced vacancies	XPS and in situ XRD	[12]
S-C <sub>2</sub> N aerogel	1.53	0.98	0.88	0.65	Unsaturated coordination sites generated from pyridinic and graphitic N species	XPS	[13]
FeCo-N-C-700	1.61	1.01	0.90	0.71	FeCo active sites; Modulated electronic properties of FeCo by N-doping	High-resolution XPS N 1s spectrum	[14]
Co-N-CNTs	1.69	0.97	0.90	0.79	Co-N-C moieties	XPS and HR-TEM	[15]
Meso-CoNC@GF	1.66	0.99	0.87	0.79	N/Co-containing active sites	HR-TEM, in-situ X-ray diffraction, and Raman spectroscopy	[16]
Fe/N/C @BMZIF	1.64	0.99	0.85	0.79	N/A	N/A	[17]
Fe@C-NG/NCNTs	1.68	0.93	0.84	0.84	Fe@C structure enhanced Fe-N <sub>x</sub>	XPS, <sup>57</sup> Fe Mössbauer transmission spectra and EXAFS spectra	[18]
CoZn-NC-700	1.62	0.98	0.84	0.78	N- and metal-based species	XPS, HR-TEM, and poisoning experiment with KSCN and EDTA	[19]
CoO <sub>x</sub> @NGCR	1.74	0.91	0.80	0.94	Pyridinic N for ORR, graphitic N for the adsorption of oxygen molecules, Co-N active sites	HR-TEM, XPS	[20]
Co/Co <sub>x</sub> S <sub>y</sub> @SNCF-800	1.536	0.83	0.74	0.796	Co/Co <sub>x</sub> S <sub>y</sub> and suitable S <sub>n</sub> N codoping in the carbon structure	TEM, XPS	[21]
NC-Co <sub>3</sub> O <sub>4</sub> -90	1.588	0.91	0.87	0.718	Co <sub>3</sub> O <sub>4</sub>	Ex-situ STEM-EELS spectrum	[22]

and the easier oxidation of the more open (100) facet. In Figure 1a,b, the terminations of the (110) and (100) surfaces are shown and the active metal cus ( $M_{cus}$ : Ir and Ru) sites are marked. Concerning the stability of these state-of-the-art catalysts, Mayrhofer and co-workers revealed an opposed trend between the OER stability and activity for these catalyst surfaces in alkaline medium.<sup>[26]</sup>

Even though Pt and Ir/Ru oxides are the best catalysts towards the ORR and the OER, respectively, their abilities to catalyze both reactions are limited. The reason behind this is the formation of insulating Pt oxides during the OER on the one side,<sup>[28]</sup> and the reduced ORR activity of IrO<sub>2</sub> and RuO<sub>2</sub> on the other side.<sup>[29]</sup> Moreover, the scarcity and high cost limit large-scale applications and motivated the search for alternatives.

Promising alternatives are rutile-type oxides such as MnO<sub>2</sub>, NiO<sub>2</sub> and spinel-type oxides such as Co<sub>3</sub>O<sub>4</sub>, Fe<sub>3</sub>O<sub>4</sub>. Here, the structure and oxidation state of the active phase can both tune the ORR and OER activities. For example, Jaramillo and co-workers conducted an in-situ X-ray absorption spectroscopy (XAS) measurement to access the active phase of MnO<sub>x</sub> bifunctional thin film catalysts. The technique is explained in further detail in section 7. The authors observed a spinel-like structure of a disordered Mn<sub>3</sub>O<sub>4</sub> phase (*cf.* Figure 1c,d) under ORR conditions. Under OER conditions, 80% of the catalyst changed to an oxidized MnO<sub>x</sub> phase resembling a birnessite structure (*cf.* Figure 1c,e). By a variation in the thickness of the thin film (green and purple curves in Figure 1c refer to 100 nm and 200 nm film thickness), it was found that the OER is not restricted to the surface of the film but can proceed throughout the porous thin film.<sup>[27]</sup>

## 2.2. Mixed Transition Metal Oxides

Going from single-metal oxides to homogenous metal mixing can alter inherent electronic and/or structural properties of the host material in order to achieve higher activities. The most prominent mixed transition metal oxides possess a spinel or perovskite structure.<sup>[30–32]</sup> Spinel oxides (A<sub>x</sub>B<sub>3-x</sub>O<sub>4</sub>) have two types of metal sites: the tetrahedral sites and the octahedral sites. The latter are regarded as more active in oxygen electrocatalysis.<sup>[33]</sup> Perovskite oxides, on the other hand, possess the general formula ABO<sub>3</sub>, where A and B are cations of different sizes (A is larger than B).<sup>[34]</sup> Figure 2a shows the cubic crystal structure of perovskites. Besides the cubic structure, also less symmetric tetragonal or orthorhombic structures exist. Partially substituting the cations on the A- or the B-site with a different metal can have different effects on the catalytic performance, as explained in the following using studies on thin films as examples.

It was stated that substituting the B-site of ABO<sub>3</sub> perovskite catalysts can significantly influence both the catalytic activity and stability.<sup>[37]</sup> As an example, LaNiO<sub>3</sub> thin films have been doped with Fe in the form of LaNi<sub>1-x</sub>Fe<sub>x</sub>O<sub>3</sub> where x=0, 0.1, 0.2, 0.6.<sup>[35]</sup> As shown in Figure 2b,c doping with Fe was beneficial for both the ORR and OER activity. Corroborated with field-emission scanning electron microscopy (FESEM) and X-ray photoelectron spectroscopy (XPS), the authors assign the benefit of the partial substitution of Ni with Fe to a higher amount of adsorbed hydroxyl (OH<sup>-</sup>) and to stabilization of Ni<sup>III</sup> species on the surface. Both are beneficial for both the OER and ORR activities.<sup>[38,39]</sup> Thus, the LaNi<sub>0.8</sub>Fe<sub>0.2</sub>O<sub>3</sub> catalyst does not only show superior OER and ORR activity but is also stable within

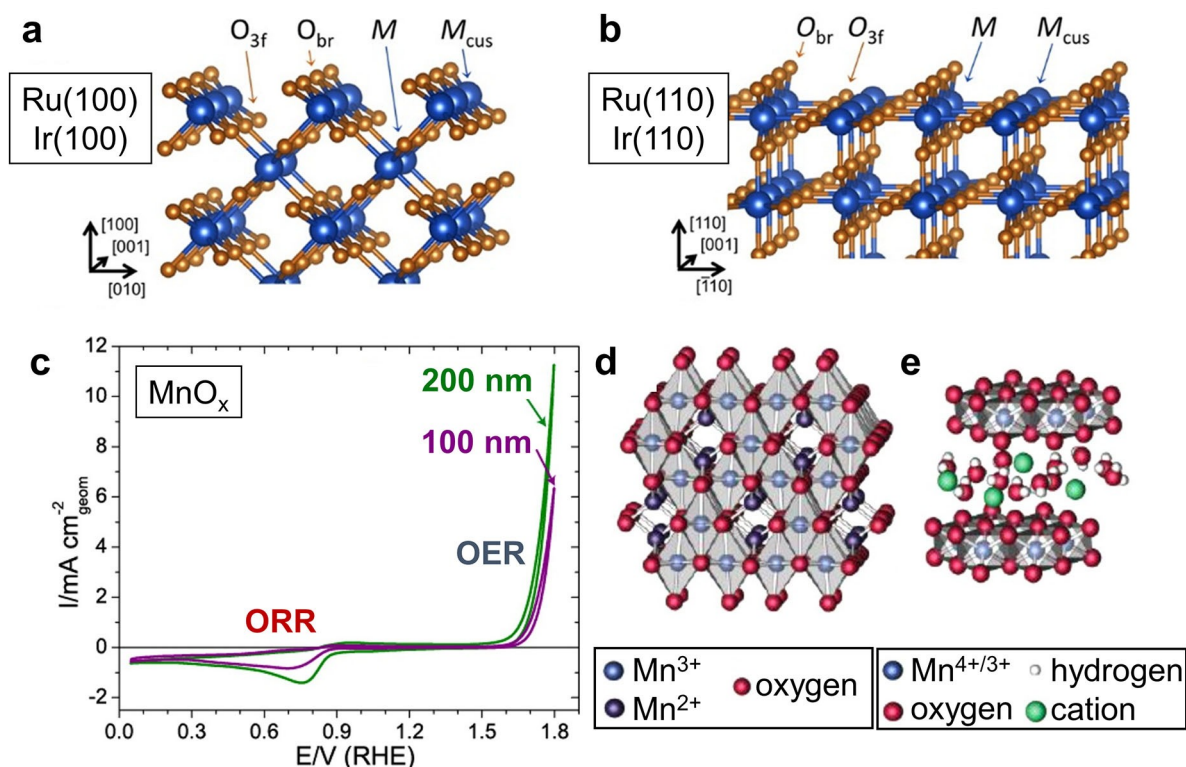


**Figure 1.** Active sites of monometallic oxide catalysts. **a, b**) State-of-the-art OER catalysts rutile  $\text{RuO}_2$  and  $\text{IrO}_2$ . In alkaline medium, active sites have been assigned to the coordinatively undersaturated metal sites ( $M_{\text{cus}}$ ). Due to the higher density of  $M_{\text{cus}}$  sites and the more open structure, the (100) surface outperforms its (110) counterpart. Reprinted with permission from Ref. [25]. Copyright (2014) ACS. **c**) The ORR and the OER activity of bifunctional  $\text{MnO}_x$  thin-film catalysts. In-situ X-ray absorption spectroscopy revealed that the active phase changed from **d**) spinel-type  $\text{Mn}_3\text{O}_4$  during the ORR to **e**) an oxidized  $\text{MnO}_x$  phase resembling a birnessite structure under OER conditions. Adapted with permission from Ref. [27]. Copyright (2013) ACS.

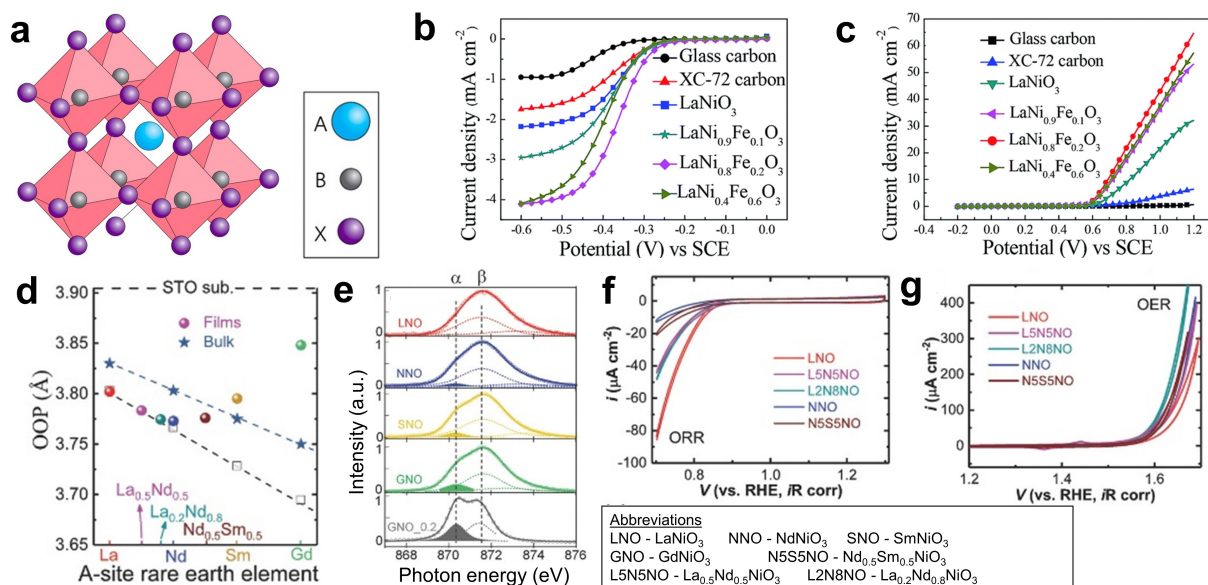


**Figure 2.** Bifunctional perovskite oxides catalysts. **a**) Crystal structure of a cubic perovskite  $\text{ABX}_3$ , where A and B are cations of different sizes, and X is oxygen in the case of OER/ORR bifunctional catalysts. Reprinted with permission from Ref. [34]. Copyright (2014) Springer. **b, c**) The B-sites of the perovskites are considered as the active sites. Therefore, the optimization of the B-site is beneficial for both **b**) ORR and **c**) OER. Reprinted with permission from Ref. [35]. Copyright (2015) The Royal Society of Chemistry. **d–g**) The A-site, in turn, can be used to balance OER and ORR. A set of epitaxial rare-earth nickelates ( $\text{RNiO}_3$ ) have been investigated in regards to **d**) structure using the out-of-plane (OOP) lattice parameter obtained from XRD and **e**) electronically via XAS on the Ni L-edge. With a combination of structure and electronic information, trends in the **f**) ORR and **g**) OER activity can be explained. Please refer to the main text for more details. Reprinted with permission from Ref. [36]. Copyright (2018) Wiley.

300 cycles between a potential of  $-0.2$  to  $1.2 V_{SCE}$ . A higher amount of Fe ( $x=0.6$ ) was claimed to lead to the formation of NiO on the surface, which is detrimental towards catalyzing the ORR and OER.<sup>[35]</sup>

Tuning the A-site of the perovskite oxide catalyst can assist in balancing the OER and ORR activities. By assessing and comparing the structural and electronic properties of a series of epitaxial rare-earth nickelates (RNiO<sub>3</sub>) thin films, Wang and co-workers<sup>[36]</sup> were able to explain trends in the OER and ORR activities. The structure of the films was probed with X-ray diffraction (XRD), and the thereby obtained out-of-plane lattice parameters (OOP) are shown in Figure 2d. The lattice parameters of the substrate and of the bulk films are given as dashed line and star-shaped symbols, respectively. The discrepancies in lattice parameters were expected to lead to in-plane strain and a decrease in OOP lattice spacing. The prediction of the thin film lattice parameter is given as squares. Some RNiO<sub>3</sub> films are in line with the prediction. However, the OOPs of the Sm and Gd perovskites are larger than their bulk values, which was ascribed to the presence of oxygen vacancies in the film. Such oxygen vacancies will lead to a change in the oxidation state of the Ni species from  $+3$  to  $+2$ . The increasing presence of Ni<sup>2+</sup> with increasing rare earth ionic radius was confirmed by probing the Ni L edge with XAS. As shown in Figure 2e, the ratio of the “ $\alpha$ ”-species, which were directly related to the Ni<sup>2+</sup> species, increased with increasing rare earth ionic radius. The ORR activity (Figure 2f) decreased linearly with the rare-earth ionic radius. This was among other explanations assigned to the largest radius of La in RNiO<sub>3</sub> possessing the strongest covalency of the Ni–O bond which was predicted to be beneficial for the ORR.<sup>[38]</sup> The OER activity showed a more complex trend (Figure 2g) with a maximum at La<sub>0.2</sub>Nd<sub>0.8</sub>NiO<sub>3</sub>. The higher OER activity of La<sub>0.2</sub>Nd<sub>0.8</sub>NiO<sub>3</sub> was explained by the creation of oxygen vacancies accompanied by a partial reduction of Ni<sup>3+</sup> to Ni<sup>2+</sup> species, which were stated to increase the average occupancy of the e<sub>g</sub> antibonding orbital to more than one.<sup>[39]</sup>

An alternative approach for tuning a certain compound to serve as a bifunctional catalyst for both the OER and ORR is based on a hybrid method, where two different catalyst materials for the OER and ORR are combined. As an example, well-defined thin films were fabricated by a PLD method. Hereby, two state-of-the-art materials for the OER and ORR, Ba<sub>0.5</sub>Sr<sub>0.5</sub>Co<sub>0.8</sub>Fe<sub>0.2</sub>O<sub>3- $\delta$</sub>  (BSCF) and La<sub>0.8</sub>Sr<sub>0.2</sub>MnO<sub>3- $\delta$</sub>  (LSMO), respectively, were layered on top of each other according to LSMO|BSCF|substrate (001). Partial coverage of the BSCF thin film by LSMO enhanced both the OER and ORR activities compared to the respective “raw” materials.<sup>[40]</sup>

Another study aimed to elucidate the structure-activity relations of the OER was performed on strontium ruthenate (SrRuO<sub>3</sub>) single-crystal thin films. The authors reveal a close connection between stability and activity, meaning that the most active crystal facet is the least stable and *vice versa*. They suggest that the electrochemical corrosion of Ru leads to the development of “active sites”, such that the OER activity depends on electronic effects but also on the defect density on the surface.<sup>[41]</sup>

### 2.3. Carbon-based Catalysts

Carbon-based materials are promising bifunctional catalysts due to their specific high surface area, electrical conductivity, and economic viability.<sup>[42,43]</sup> It is believed that pure “defect-free” carbon materials such as carbon blacks, carbon nanotubes, and graphene possess insufficient ORR activity due to the reaction proceeding *via* a two-electron pathway.<sup>[44,45]</sup> In many studies, the active sites of pure carbon-based materials have been assigned to step and defect sites in the case of the ORR.<sup>[46–53]</sup> The OER active sites have been less studied, which may be due to carbon corrosion interfering with the catalysis.<sup>[37,53]</sup> Still, literature studies conclude that defects such as deviations in the ring structure and step edges are beneficial for the OER.<sup>[11,51,53]</sup> As an example, Yao and co-workers studied the OER and ORR activities of defective graphite to understand the underlying principles.<sup>[11]</sup> As sketched in Figure 3a, the carbon catalyst was prepared by removing the nitrogen atoms stemming from an N-doped precursor. After removing the nitrogen atoms, the reconstruction of the carbon lattice leads to defects such as “new” carbon ring forms, *i.e.*, pentagons, heptagons, and octagons. Both the ORR and OER performances were tested using linear scan voltammograms (LSVs) as shown in Figure 3b,c. The electrolyte was 0.1 M KOH saturated with O<sub>2</sub>. The catalysts were compared to state-of-the-art catalysts Pt/C and Ir/C for ORR and OER, respectively. It turned out that the defective carbon catalysts (DG) outperformed their undoped and N-doped counterparts. Besides, the authors report good stability of the DG catalysts. They ascribe the superior performance of the catalyst for both ORR and OER to ring defects, such as shown in Figure 3d-f. It was thus confirmed that defect sites are active for both OER and ORR. While this particular study<sup>[11]</sup> relies on the additional information from DFT calculations, section 7 of this review introduces techniques that are able to elucidate active sites purely experimentally. As an example, Haid *et al.* recently confirmed step edges and defects as active sites on graphite materials for both OER and ORR.<sup>[51]</sup> The authors used an *in-situ* scanning probe method, which is introduced in section 7.

It is a common approach to enhance both the ORR and OER activities by heteroatomic doping of carbon catalysts with nitrogen (N), phosphorus (P), sulfur (S), or boron (B).<sup>[54–57]</sup> The success of the introduced heteroatoms is often ascribed to their higher electronegativity compared to carbon, which eases oxygen adsorption.<sup>[58,59]</sup> However, most studies related to carbonaceous oxygen catalysts focus on nanomaterials. Little is reported on thin film or other extended model surfaces. An example of such a study is the N-doping of highly oriented pyrolytic graphite (HOPG). O’Hayre and co-workers analyzed the structural and chemical changes in HOPG upon impinging with a nitrogen ion beam.<sup>[60]</sup> At low dosage, they only report structural damages to the HOPG. Sufficient incorporation of nitrogen can only be achieved at higher dosages of *ca.*  $1 \times 10^{16}$  ions/cm<sup>2</sup>. Moreover, they probed the number of nitrogen functionalities present on the surface in, *e.g.*, the graphitic, pyridinic, and pyrrolic form. Dai and co-workers performed another study on extended surfaces.<sup>[61]</sup> The authors doped

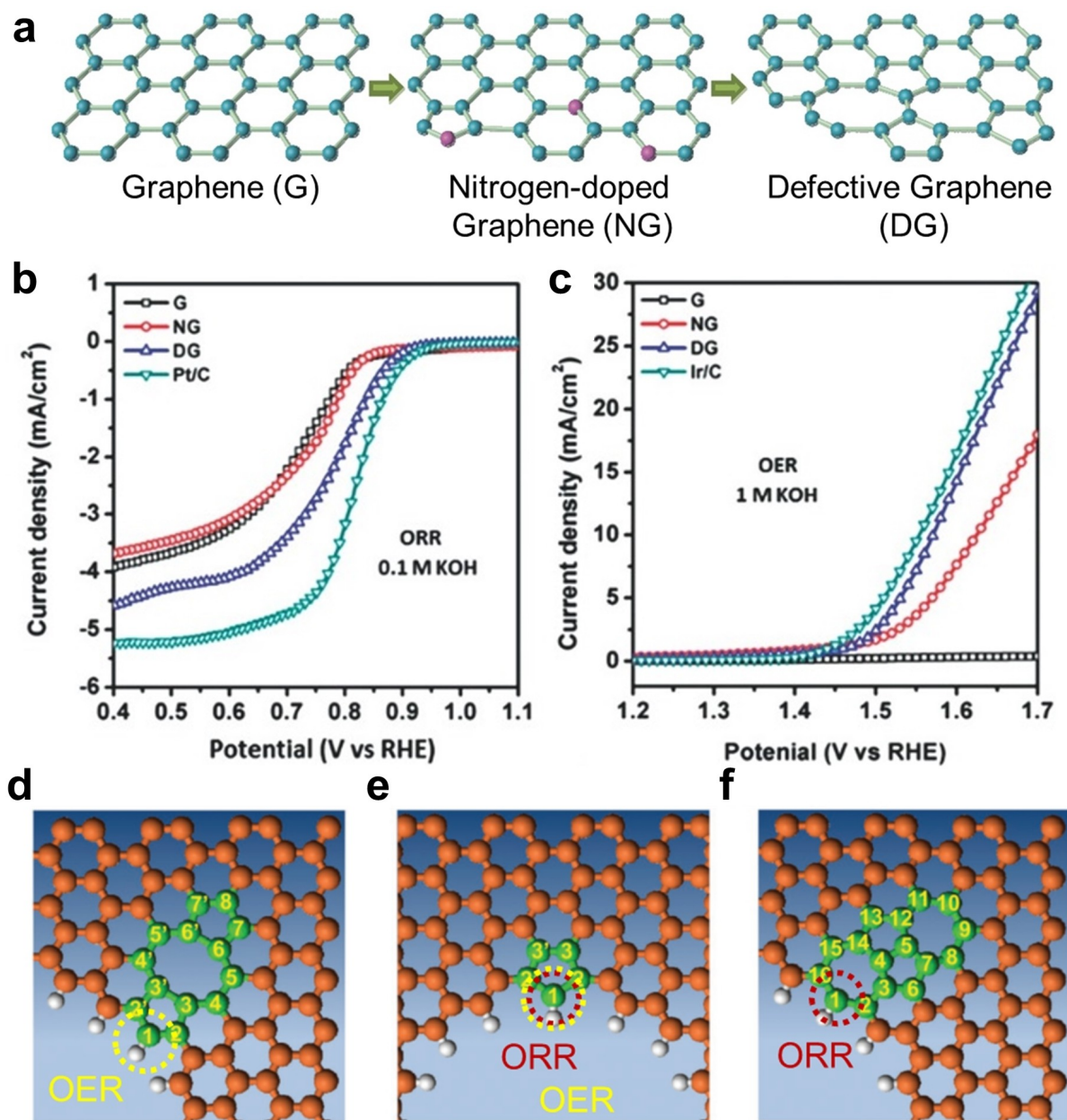


**Figure 3.** Carbon-based bifunctional catalysts. The activity of graphene surfaces can be enhanced by the incorporation of defect sites. **a)** In this study, graphene (G) was doped with nitrogen atoms (NG). Subsequently, defects were introduced by removing the N atoms. This led to a reconstruction of the carbon lattice and new ring structures such as pentagons, heptagons, and octagons. The hereby-created defective graphite (DG) catalyst showed superior **b)** ORR and **c)** OER performance. **d–f)** Postulated active sites in the defective carbon catalyst as predicted by DFT. Reprinted with permission from Ref. [11]. Copyright (2016) Wiley.

graphene sheets with nitrogen by chemical vapor deposition (CVD). They reported superior activity and stability compared to a commercial Pt/C catalyst in an alkaline medium. Furthermore, they report the presence of pyridine and pyrrolic nitrogen species. Generally speaking, in the case of N-doping of graphene, active centers for the ORR were ascribed to graphitic-N (quaternary-N), pyridinic-N, and pyrrolic-N sites.<sup>[61]</sup> In this regard, Ruoff and co-workers claim that pyridinic N species can change the ORR onset potential, whereas graphitic N can improve the limiting current density.<sup>[62]</sup> However, controversy exists upon which species plays the most important role.<sup>[63]</sup> It is

believed that the N-doping can promote a more favorable four-electron pathway for the ORR.<sup>[64,65]</sup> Active sites for the OER on N-doped carbons were assigned to the electron-withdrawing pyridinic N-sites.<sup>[66]</sup>

Besides the heterogeneous doped carbon materials discussed here, also more complex carbon catalysts are promising, such as metal-carbon hybrids of all kinds. As an example, Maruyama and co-workers report Fe–N doped carbonaceous thin films as bifunctional catalysts for both OER and ORR.<sup>[67]</sup> As further metal-carbon hybrid systems are beyond the scope of

this review, we recommend Ref. [25], Ref. [45], Ref. [68] for further reading.

### 3. MOF-based Bifunctional Electrocatalysts

Over the past decades, MOFs constructed by coordination bonds between metal nodes and organic ligands have drawn extensive attention.<sup>[69–71]</sup> They possess several unique advantages such as low density, large surface area, tunable pore size, and structural flexibility. Consequently, a significant number of studies investigated MOFs and their derivatives as potential bifunctional ORR and OER electrocatalysts.<sup>[72,73]</sup> Strategic development of MOF-based bifunctional electrocatalysts can be grouped as follows: 1) Highly efficient transition metal-nitrogen-carbon active sites can be produced by using MOFs as the sacrificial templates,<sup>[74–76]</sup> 2) Intrinsically conductive MOFs, which can achieve rapid electron transfer and high utilization of active sites through conductive ligands,<sup>[10,77]</sup> 3) MOF-derived metal-free carbon, especially heteroatom-doped carbon (e.g., N, O, S, P, and B), which exhibits ultrahigh electrochemical stability and catalytic activity during the oxygen electrocatalysis.<sup>[78,79]</sup>

To gain deeper insight into the catalytic mechanisms, it is of essence to elucidate the nature of the active sites. Extensive studies examined the reaction pathways on the catalyst surface *via* series of *ex-situ* and *in-situ* experimental techniques.<sup>[80–83]</sup> Recently, the rapid development of MOFs and MOF-derived bifunctional electrocatalysts facilitated the understanding of the electrocatalytic active sites.<sup>[84–86]</sup>

A transition metal-nitrogen-carbon structure embedded in the MOF-derived carbon matrix has been considered as one of the most promising ORR catalysts, mainly due to their high activity towards the O<sub>2</sub> adsorption and intermediate O=O bond breaking.<sup>[86,87]</sup> Moreover, the development of MOFs offers a variety of options for the synthesis of heteroatom-doped carbon. The target atoms cannot only be pre-introduced into MOFs *via* the design of organic ligands or the addition of guest molecules but can also be incorporated into the carbon matrix during the pyrolysis process.<sup>[88,89]</sup> Using these highly dispersed heteroatoms, the local electronic structure of the oxygen catalysts can be tailored to increase their catalytic efficiency.<sup>[16]</sup> In recent studies, MOF-derived single-atom metal M–N–C catalysts have been widely investigated, and the corresponding active sites have been gradually revealed from the evidence of physicochemical techniques.<sup>[90,91]</sup> For example, Li and co-workers proposed a novel MOF@polymer strategy for the synthesis of single iron atomic sites, which were highly dispersed in the nitrogen, phosphorus, and sulfur co-doped hollow carbon polyhedron (denoted as Fe-SAs/NPS-HC).<sup>[92]</sup> As shown in Figure 4a, the homogeneous spatial distribution of single iron atomic sites was confirmed by the aberration-corrected high angle annular dark-field scanning transmission electron microscopy (HAADF-STEM). Moreover, the presence of isolated Fe atoms coordinated with four N atoms as Fe–N<sub>4</sub> structure was proven *via* X-ray absorption fine structure (XAFS) fitting curves. The schematic illustration of the Fe–N<sub>4</sub> structure is displayed in Figure 4b. Benefiting from the unique coordinated structure

and atomic dispersion, Fe-SAs/NPS-HC catalyst exhibited impressively high activity in the Zn-air battery, achieving a maximum power density of 195.0 mW cm<sup>-2</sup>.<sup>[92]</sup> Besides the Fe–N<sub>4</sub> structure, MOF-derived Co–N–C materials usually possess remarkable catalytic activity towards the ORR/OER, and the Co–N structure has been regarded as the main active site. For instance, Fu and co-workers designed a 3D hierarchical structure where the Co nanoislands were rooted on Co–N–C nanosheets (denoted as Co/Co–N–C).<sup>[90]</sup> The electronic structure and coordination properties were investigated *via* extended XAFS spectra, revealing the existences of Co–N and Co–Co structures. *Operando* XAFS further confirmed the ORR/OER catalytic mechanisms using Co/Co–N–C catalyst in a Zn-air battery under the electrochemical reaction conditions. As shown in Figure 4c, the positive energy shifts of the absorption edge of Co K-edge manifest the correlation between Co oxidation state and the applied potential, corresponding to the adsorption of oxygen-containing intermediates. Figure 4d displays the Co K-edge FT-EXAFS spectroscopy. When the applied potential increased, the intensity of the Co–N bond located at ≈1.3 Å gradually decreased, whereas the intensities of the Co–O bond (at ≈1.5 Å) and Co–Co bond (at ≈2.2 Å) increased. Note that the new peak at ≈2.5 Å appeared and increased with the increase of potential, which is assigned to the high oxide state of Co in Co–Co bond during the OER. The shortened Co–Co and Co–N bond lengths infer their important role for the ORR. In turn, the increased Co–O bond length indicates that the Co–O is the active site for the OER. Jaouen and co-workers also prepared the pyrolyzed Co–N–C materials and identified the porphyrin-like CoN<sub>4</sub>C<sub>12</sub> moiety as the active sites towards the ORR by X-ray absorption near-edge structure (XANES) spectroscopy.<sup>[86]</sup> The *operando* XANES spectra (Figure 4e and f) were measured as a function of the ORR potential for the Co–N–C and Fe–N–C catalysts in an N<sub>2</sub>-saturated electrolyte. A drastic change of the normalized XANES spectra can be found in Fe–N–C with the increased electrochemical potential, while no significant change was detected in Co–N–C. This result was attributed to the changes in the oxidation state, conformation, and/or the spin state of Fe–N–C.

In order to overcome the shortcoming of low electrical conductivity, conductive MOFs have been developed through the construction of π-conjugated pathways.<sup>[10,77,93]</sup> Benefiting from the intrinsic advantages of MOFs (such as well-defined porous structure, ultrahigh specific surface area, and abundant unsaturated metal centers), these conductive MOFs exhibit remarkable bifunctional OER/ORR catalytic performance. Dincă and co-workers performed pioneering work by designing a 2D conductive MOF, Ni<sub>3</sub>(HITP)<sub>2</sub> (HITP = 2,3,6,7,10,11-hexaiminotriphenylene), as a highly efficient ORR catalyst (Figure 5a).<sup>[77]</sup> The 2D Ni<sub>3</sub>(HITP)<sub>2</sub> with a conjugate coplanar structure achieved a superior electrical conductivity (σ = 40 S cm<sup>-1</sup>) and a competitive onset potential of 0.82 V at the current density of –50 μA cm<sup>-2</sup>. In their subsequent work, the active sites of the conductive MOFs for catalytic O<sub>2</sub> reduction were identified on the ligand rather than the metal by using the kinetic and XAS data. Recently, a series of ultrathin MOFs with coordinated unsaturated metal sites or lattice strains have been developed

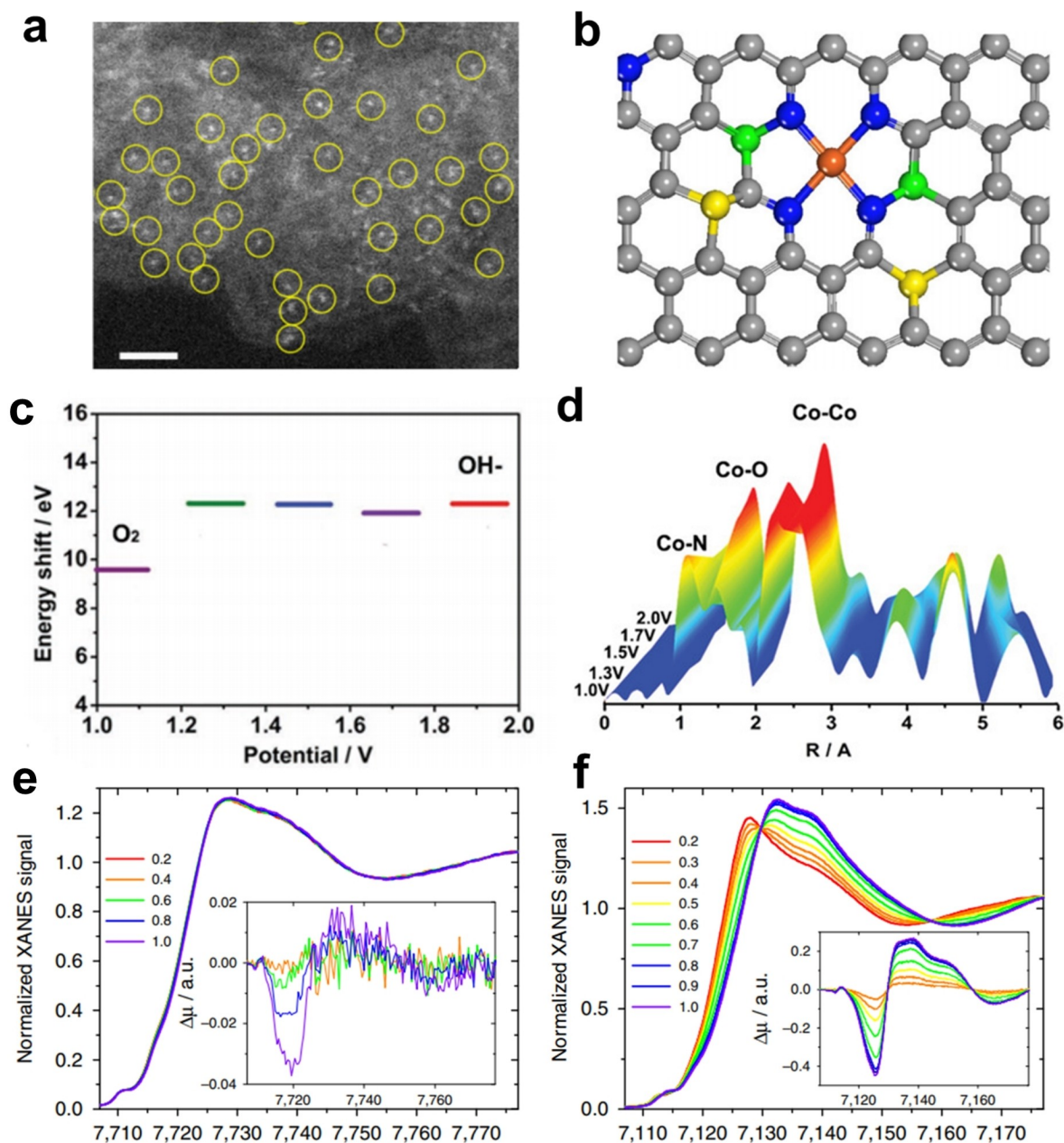


**Figure 4.** a) Aberration-corrected (AC) HAADF-STEM image showing the single iron atom in the Fe-SAs/NPS-HC catalyst. Scale bar: 1 nm. b) Schematic illustration of the Fe-SAs/NPS-HC structure, Fe = orange, N = blue, S = yellow, P = green, and C = grey. Reprinted with permission from Ref. [92]. Copyright (2018) Springer. c) Co K-edge energy shift of XANES of Co/Co-N-C measured as a function of the electrochemical potential and d) EXAFS spectra for the length changes of the Co-N, Co-O, and Co-Co bonds at the Co K-edge with the potential increase. Reprinted with permission from Ref. [90]. Copyright (2019) Wiley. e and f) Normalized operando XANES spectra of the Co-N-C and Fe-N-C catalysts measured at various potentials. Reprinted with permission from Ref. [86]. Copyright (2017) Springer.

as highly active bifunctional ORR/OER catalysts. For instance, Liu and co-workers synthesized lattice-strained NiFe MOFs *via* a controllable step to photo-induce lattice strain.<sup>[94]</sup> The as-prepared bifunctional catalysts achieved outstanding mass activities of 500  $\text{Ag}_{\text{metal}}^{-1}$  at a 0.83 V half-wave potential for the ORR and 2000  $\text{Ag}_{\text{metal}}^{-1}$  at an overpotential of 300 mV for the OER (Figure 5b, c, and d), which were comparable to those of commercial Pt/C and  $\text{RuO}_2$ . The high-valence  $\text{Ni}^{4+}$  species with crucial superoxide,  $^*\text{OOH}$ , intermediate were determined as the real active sites by cutting-edge *operando* synchrotron

radiation Fourier transform infrared (SR-FTIR) spectroscopy and XAS. As shown in Figure 5e, the  $\text{Ni}^{4+}$  feature peak that emerged at 0.8 V in the Ni  $L_{3,2}$ -edge XANES spectra was proportional to the stretching vibration of superoxide ( $-\text{O}-\text{O}-$ ) obtained from the *operando* SR-FTIR measurements. The  $\text{Ni}^{4+}/\text{Ni}^{2+}$  ratio gradually increased with the abatement of the potential from 0.8 to 0.6 V, which is in good agreement with the infrared signal of  $-\text{O}-\text{O}-$ . Similar results can be found for the OER process (Figure 5f). Accordingly, the close association between the generation of surface superoxide intermediates and the

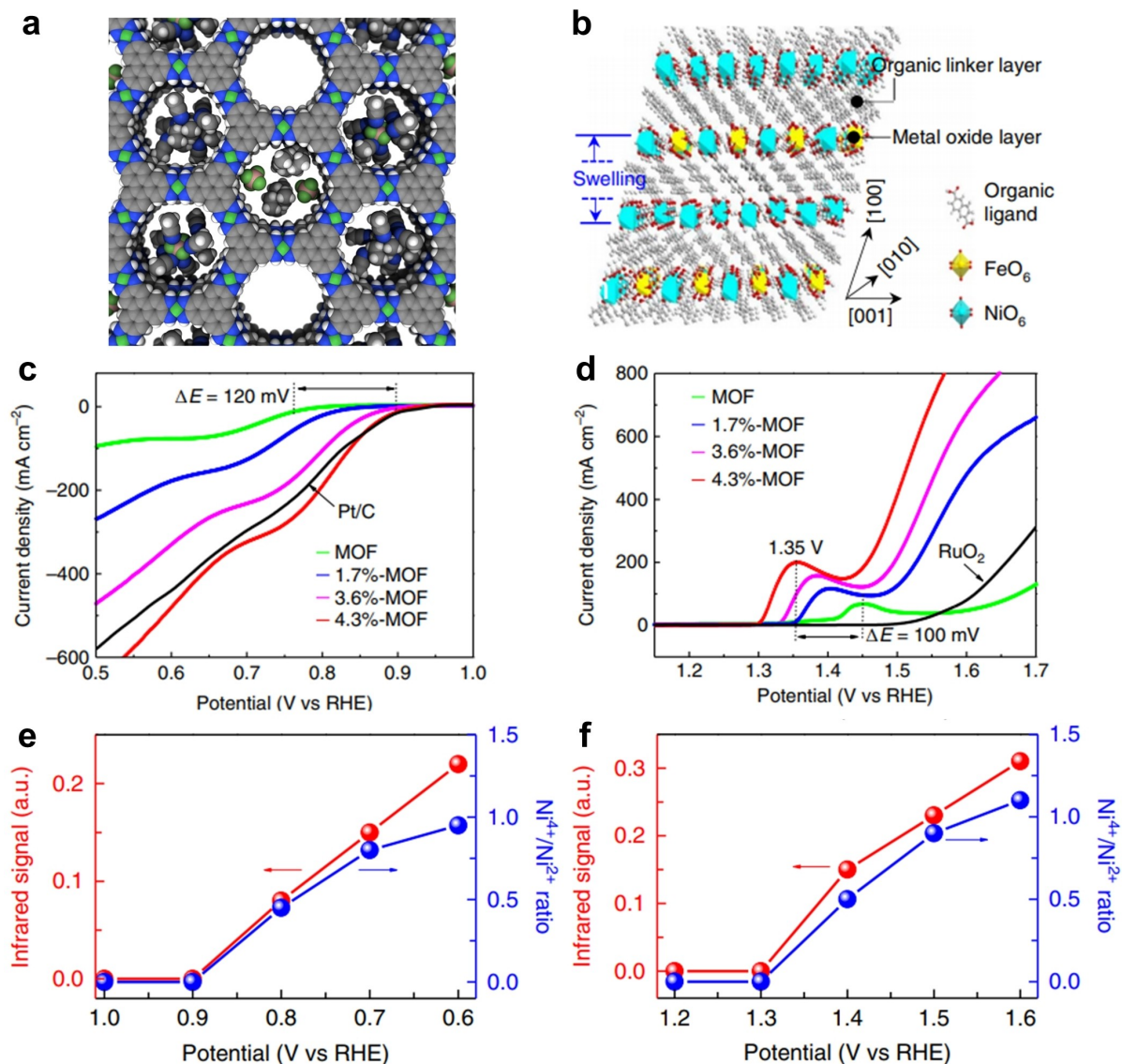


**Figure 5.** a) Schematic of the relative pore size in the idealized Ni<sub>3</sub>(HITP)<sub>2</sub>. Pores were filled by electrolyte Et<sub>4</sub>N<sup>+</sup> and BF<sub>4</sub><sup>-</sup> ions and acetonitrile solvent molecules. Reprinted with permission from Ref. [77]. Copyright (2016) Springer. b) Crystal structure of NiFe MOFs; c and d) ORR and OER polarization curves of the pristine, 1.7%-, 3.6%- and 4.3%-MOFs and commercial Pt/C or RuO<sub>2</sub> in 0.1 M KOH; e and f) Infrared signal at 1,048 cm<sup>-1</sup> and Ni<sup>4+</sup>/Ni<sup>2+</sup> ratio as a function of applied potential for the 4.3%-MOF during the ORR and OER. Herein, the 1.7%, 3.6% and 4.3% represent lattice expansion ratios in the MOFs. Reprinted with permission from Ref. [94]. Copyright (2019) Springer.

emergence of Ni<sup>4+</sup> revealed the critical role in the high-efficiency 4e<sup>-</sup> oxygen electrocatalytic process.

Additional approaches, such as X-ray diffraction (XRD), Raman spectroscopy, and X-ray photoelectron spectroscopy (XPS), are widely accepted to *in-situ* observe the active sites of MOFs and MOF derivatives during the electrocatalytic process.<sup>[16,95,96]</sup> These advanced analytical techniques can sensitively probe the changes in the lattice parameters, chemical composition, chemisorption/desorption of oxygen molecules, and oxygen-containing intermediates, providing a deeper understanding of the reaction mechanism. For example, Yan and co-workers comprehensively investigated the oxygen chemisorption processes on a heteroatom-doped carbon material by *in-situ* XRD and Raman spectroscopy.<sup>[16]</sup> MOF-

derived mesoporous CoNC nanocrystal-supported on the graphene framework (denoted as MesoCoNC@GF) was prepared by annealing treatment, exhibiting an ultra-low overpotential of 0.79 V between the potential at a current density of 10 mA cm<sup>-2</sup> (E<sub>j=10</sub>) of the OER and the half-wave potential (E<sub>1/2</sub>) of the ORR (Figure 6a). The reaction mechanism of MesoCoNC@GF in a Zn-air battery was evaluated through *in-situ* XRD spectra (Figure 6b). There were two major diffraction peaks at ca. 44° and 54° in the original state of the air cathode, corresponding to the carbon. Note that using MesoCoNC@GF as the air cathode in a Zn-air battery, the two peaks from the carbon gradually became weaker during the discharging process, which can be attributed to the influence of heteroatom dopants on carbon. In nitrogen-doped carbon materials, nitrogen dopants, having higher

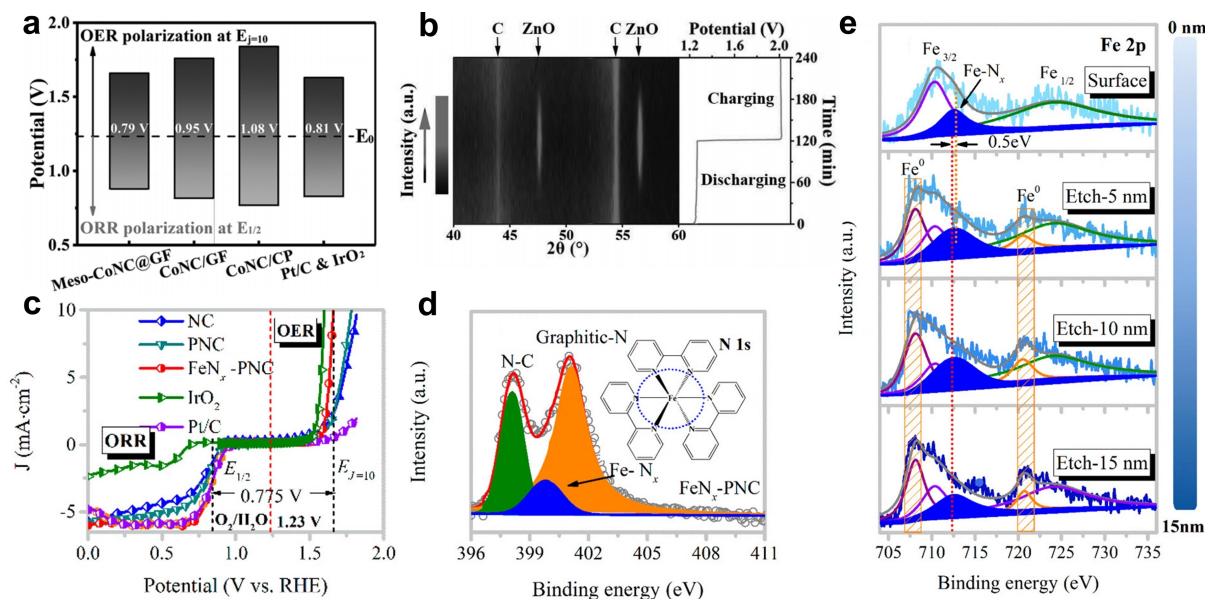


**Figure 6.** a) The potential differences between the half-wave potential  $E_{1/2}$  of the ORR and the potential at the current density of  $10 \text{ mA} \cdot \text{cm}^{-2}$  ( $E_{j=10}$ ) of the OER for the CoNC based catalysts and commercial Pt/C + IrO<sub>2</sub> catalysts and b) XRD intensity map of Zn-air battery with Meso-CoNC@GF air cathode during the charging and discharging processes. Reprinted with permission from Ref. [16]. Copyright (2017) Wiley. c) The OER and ORR polarization curves, the  $E_{1/2}$  of ORR and  $E_{j=10}$  of OER are marked by dotted lines for the comparison of bifunctional catalytic activities; d) High-resolution XPS spectrum of N 1s for the FeN<sub>x</sub>-PNC; e) The XPS depth profiles of Fe 2p for the FeN<sub>x</sub>-PNC at different etching depths (0–15 nm). Reprinted with permission from Ref. [96]. Copyright (2018) ACS.

electronegativity, can lead to electron deficiencies of the adjacent carbon atoms. This further accelerates the chemisorption of oxygen molecules and the generation of oxygen-containing intermediates on the carbon material occurring under a lower ORR overpotential. In addition, Zhi and co-workers proposed a strategy to synthesize single-site dispersed Fe–N<sub>x</sub> species on 2D porous nitrogen-doped carbon (denoted as FeN<sub>x</sub>-PNC), achieving a small potential difference value of 0.775 V between the  $E_{j=10}$  of the OER and the  $E_{1/2}$  of the ORR (Figure 6c).<sup>[96]</sup> Subsequently, XPS measurements were conducted to reveal the coordinated structures of Fe–N<sub>x</sub> moieties. As shown in Figure 6d, the coordination of six nitrogen atoms with an iron center was confirmed *via* the peak at 399.6 eV, corresponding to the Fe–N<sub>x</sub> structure in FeN<sub>x</sub>-PNC. The Fe–N<sub>x</sub> structure has been considered as the active site for oxygen catalysis. Moreover, XPS depth profiling was performed to study the condition of Fe species on the surface and in the bulk of FeN<sub>x</sub>-PNC catalyst (Figure 6e). The results indicated that in the surface layer of the FeN<sub>x</sub>-PNC catalyst, a positive shift of the Fe–N<sub>x</sub> configuration peak at around 712.4 eV could be found in comparison with the bulk, demonstrating lower charge density on the central Fe in surface components. The lower charge density is a clue of the interaction between the Fe–N<sub>x</sub> configuration and other Fe–C<sub>x</sub> components.

#### 4. Investigation of Single Nanoparticles on Nanoelectrodes

As introduced in section 2, precious metal catalysts (such as Pt, Ru, Ir), despite their high cost, are among the most important ORR and OER catalysts.<sup>[97,98]</sup> Due to their higher abundance, transition-metal oxides are explored as alternatives to replace the noble-metal-comprised materials.<sup>[99,100]</sup> However, the development of cheap, active, and stable catalysts or the optimization of the existing ones remains a challenge. To rationalize the design of optimal catalysts, it is essential to understand the fundamental mechanisms and the structure-activity relations. Common catalysts are microscopically ill-defined, with metal clusters showing wide ranges of structure and sizes. The macroscopic observation of performance reveals only ensemble-averaged properties. Subsequently, the rational improvement of materials is difficult as the activities of the individual morphology and topology features remain unclear. Studies on single nanoparticles (SNPs) with known shape and size could circumvent these difficulties and reveal particular features due to their unique structure-dependent catalytic properties. Recent investigations of SNPs in electrochemistry follow the aforementioned concept to characterize individual cluster performance and have attracted great interest.<sup>[101–104]</sup> This section presents the latest approaches involving nanoelectrodes, which can be applied for the single entity investigations on the structure-activity relationship under reaction conditions.

In the absence of mass-transfer limitations, conducting kinetic measurements over a single particle supported on the nanoelectrode reveals more reliable information than the rotating disk electrode (RDE) studies. For instance, carbon

nanoelectrodes having very small electroactive areas with effective radii of only a few nanometers are the ideal model electrode system for investigating the size effects of supported nanoparticles or nanocrystals of electrocatalysts.<sup>[105]</sup> Another important feature of single-particle measurements is the insignificant contribution of the background current, as its contribution depends on the electrode area.

Recently, the OER was investigated over differently sized Ni(OH)<sub>2</sub> SNPs supported on carbon nanoelectrodes. Carbon nanoelectrodes (CNE) were produced by laser pulling of a quartz capillary into a nanopipette, followed by filling the nanopipette tip with the pyrolytic carbon. The single nanoparticle of Ni(OH)<sub>2</sub> was electrochemically deposited on the electrode tip from the NiCl<sub>2</sub> solution.<sup>[106]</sup> The radii of the deposited nanoparticles with approximately spherical geometry varied in the range of 20–500 nm (Figure 7a). Catalytic activity was estimated at high overpotentials to establish the dependence of the turnover frequencies (TOF) on the SNPs size. The TOF decreased with increasing the particle size (Figure 7b). Moreover, the received TOF values were found to be higher compared to data obtained on macroscopic electrodes.<sup>[107]</sup> Measurements of SNPs supported on nanoelectrodes are considered more accurate due to very high mass transport rates, good electrical connectivity without conductive additives, and a more precise evaluation of the particle size. The latter is crucial for further estimation of the active sites and the subsequent calculations of the TOF.<sup>[106,107]</sup>

SEM-controlled micromanipulator is another approach for the investigation of catalytic features of single entities on the nanoelectrodes. This robotic technique allows to select the individual particle by picking it up to support onto the surface of the CNE under SEM imaging (Figure 8). The main advantage of this “picking-and-placing” method is the control of the particle orientation on the CNE surface (Figure 8f-i).<sup>[108]</sup> Using the above-described technique, differently sized single nanoparticles of the hexagonal-shaped Co<sub>3</sub>O<sub>4</sub> supported on the CNE were investigated for the OER. The particles were synthesized by a wet colloidal synthesis, with the size variation from 180 to 300 nm.<sup>[109]</sup> The CNE was produced by the pyrolytic decomposition of butane gas inside the pulled quartz nanopipettes.<sup>[108]</sup> The individual Co<sub>3</sub>O<sub>4</sub> nanoparticles demonstrated a high

catalytic size-dependent activity towards the OER performed in an alkaline medium, as well as high TOF values of  $532 \pm 100 \text{ s}^{-1}$  at 1.92 V vs. RHE. In addition, structural changes of the single hexagonal-shaped Co<sub>3</sub>O<sub>4</sub> particles from crystalline to amorphous were observed at high anodic OER overpotentials.<sup>[108]</sup>

The methods for the investigation of the catalytic performance of single entities on the nanoelectrodes can be divided into two groups. The first one consists of steady-state techniques when the particle is immobilized on the electrode surface. The techniques presented above belong to this group.<sup>[105–107]</sup> The second group contains transient methods, which are based on the stochastic collision of the particle with the electrode.<sup>[110,111,112]</sup> However, obtaining structural information from such transient methods is still under development. Scanning electrochemical cell microscopy (SECCM) is an alternative technique for analyzing the relation between size and activity of single entities. More details on the SECCM will be provided in section 7.<sup>[104,113]</sup> Nanoelectrode techniques, investigating single active nanoparticles, prove to be powerful tools in elucidating size-specific phenomena in electrocatalysis. This will help in understanding the size-structure activity relationship at the nanoscale and consequently improve the performances of catalysts, especially for bifunctional applications.

## 5. Mass- and Size-selected Nanoparticles

As presented in section 4, much can be learned about the nature of individual particles' active sites from a focused observation of them. However, accurate measurements are often very complicated in practice due to a relatively low signal-to-noise ratio and limited reproducibility. Therefore, a highly accurate characterization of the individual particle is essential. Nonetheless, the investigation of an ensemble of particles is much closer to subsequent application, and the signal-to-noise ratios can be significantly improved. However, in this case, the measurement is usually an averaging over all investigated particles. Obviously, if there is a significant variance in size or shape of the particles, the impact with respect of individual particles is low. A widely used approach is, therefore,

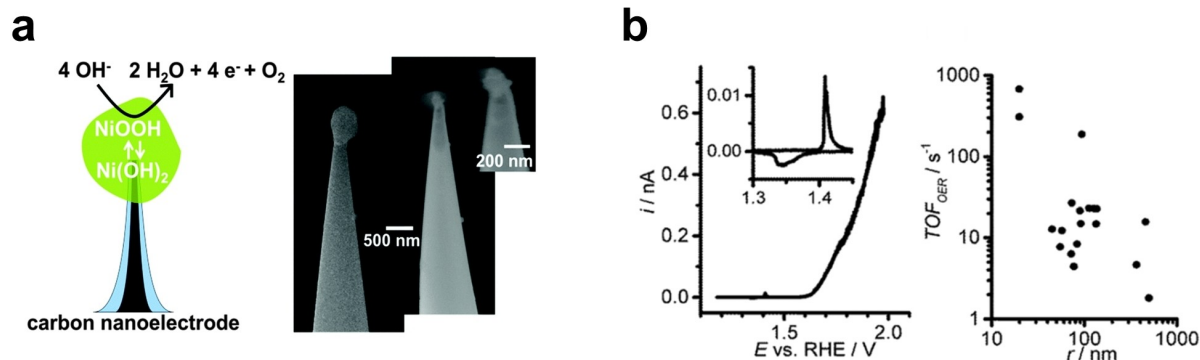


**Figure 7.** a) Scheme and SEM images of single Ni(OH)<sub>2</sub> nanoparticles supported on the carbon nano electrodes (CNE). b) Cyclic voltammogram (10 mV s<sup>-1</sup>) at a single particle electrode with  $r = 83 \text{ nm}$  in 0.1 M KOH and turnover frequencies for the OER at 1.88 V vs. RHE for particles with different sizes. Reprinted with permission from Ref. [106]. Copyright (2016) Royal Society of Chemistry.

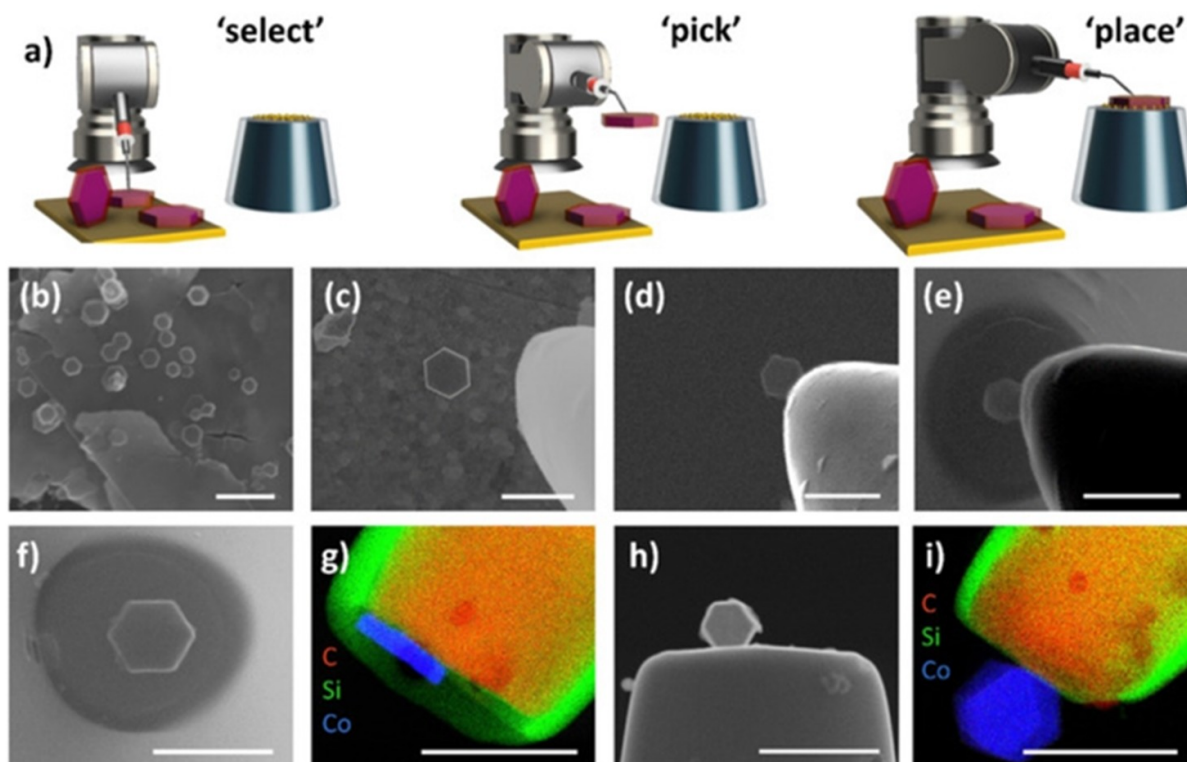


**Figure 8.** a) Schematics of the setup and b–e) SEM images of the selection, picking and placing of individual hexagonally shaped  $\text{Co}_3\text{O}_4$  nanoparticles onto the CNE surface; f, h) SEM images of differently oriented particles on the CNE. g, i) TEM-EDS elemental mapping images of the composition of the nano-assemblies presented in (f, h). Scale bars corresponding to 500 nm. Reprinted with permission from Ref. [108]. Copyright (2021) Wiley.

to investigate an ensemble of particles with well-defined and selected sizes and shapes.

G. Kwon and co-workers are among the first to synthesize size-selected clusters for the study of active sites of electrocatalysts. Among others, they have decorated electrodes with size-selected palladium nanoclusters and benchmarked their electrocatalytic performance.<sup>[114]</sup> An Si electrode coated with ultrananocrystalline diamond (UNCD) was used as the substrate due to its good corrosion resistance. By laser vaporization of a rotating Pd target, a molecular beam was generated which was guided by ion optics and a quadrupole assembly. This allowed a selection between clusters with  $4 \pm 1$ ,  $6 \pm 2$ , and  $17 \pm 3$  atoms each, denoted as  $\text{Pd}_4$ ,  $\text{Pd}_6$ , and  $\text{Pd}_{17}$ , respectively. To avoid agglomeration, these clusters were soft-landed on separate electrodes, and the surface coverage was limited to 0.1 monolayers. The interesting aspect of the study is that these nanoclusters consist of only a few or just a single catalytic site. This simplifies the identification of active sites. The electrodes were characterized before and after the electrochemical measurements by means of grazing incidence XAS (GIXAS) and grazing incidence small-angle X-ray scattering (GISAXS). An oxidation state similar to that of  $\text{PdO}$  was determined. The spectra remained unchanged within the limits of measurement accuracy even after the electrochemical experiments. The authors conclude from the nearly identical before and after spectra that they “have sintering- and leakage-resistant sub-nanometer clusters under electrocatalytic conditions”. This

holds true for the relatively short electrochemical potential cycling of this study at ambient conditions, which is essential for identifying active sites. However, no accelerated aging tests were performed to benchmark the aforementioned properties under electrolyzer conditions. Therefore, one cannot conclude the suitability of these nanocluster catalysts for real systems.

Figure 9a shows the anodic polarization curves in the OER region of the electrodes decorated with  $\text{Pd}_{17}$ ,  $\text{Pd}_6$ , and  $\text{Pd}_4$  in 1 M NaOH. For comparison, the polarization curve of the UNCD coated electrode without any Pd clusters was also recorded. The OER activity of the electrodes with  $\text{Pd}_4$  is significantly lower compared to the two electrodes with larger Pd clusters. On closer inspection, it is noticeable that the measured currents are even lower than for the substrate without Pd, and the  $\text{Pd}_4$  clusters thus block the more active support material. The larger  $\text{Pd}_6$  and  $\text{Pd}_{17}$  clusters nevertheless show a very high activity considering that the catalyst is Pd. The authors determined a TOF at  $\eta = 351$  mV per Pd atom of 0.68 and 0.60  $\text{atom}^{-1} \text{s}^{-1}$  for  $\text{Pd}_6$  and  $\text{Pd}_{17}$ , respectively. These high TOFs are even comparable to those of Ir ( $\text{TOF}_{\text{Ir}} = 0.64 \text{ atom}^{-1} \text{s}^{-1}$ ), which is considered as one of the most active OER catalysts. The transition from practically zero electrocatalytic activity for  $\text{Pd}_4$  to very high activity for  $\text{Pd}_6$  clusters is of particular importance for the determination of active sites. Here, the model character of the size-selected nanoclusters pays off. Kwon and co-workers finally identified the bridge sites of  $\text{Pd}_6$  clusters as active sites by analyzing the possible binding sites of both clusters using DFT

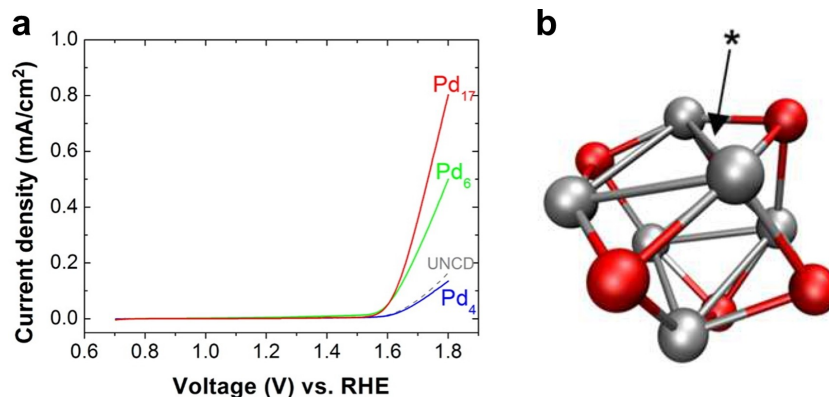


**Figure 9.** Size-selected Pd nanocluster catalysts. **a)** Anodic polarization curves of Pd clusters on UNCD recorded in the OER region in 1 M NaOH. Current densities for Pd<sub>17</sub> (red), Pd<sub>6</sub> (green), Pd<sub>4</sub> (blue), and the blank UNCD support (grey dashed line) are normalized to the geometric surface area of the electrode exposed to the electrolyte. The electrode coverage with clusters was 11.0%, 7.9%, and 9.4% for Pd<sub>17</sub>, Pd<sub>6</sub>, and Pd<sub>4</sub>, respectively. **b)** Schematic of an active site on a Pd<sub>6</sub> nanocluster. The oxidation state of all clusters was determined as ca +2. Therefore, a Pd<sub>6</sub>O<sub>6</sub> cluster was investigated. Note that one of the (red) oxygen atoms is hidden in this representation. The active site of the cluster was found as the bridge-site of two Pd atoms, highlighted with an asterisk “\*”. Reprinted with permission from Ref. [114]. Copyright (2013) ACS.

calculations. Figure 9b shows a Pd<sub>6</sub>O<sub>6</sub> cluster, the active site is marked with an asterisk “\*”.

State-of-the-art precious metal-free bifunctional OER/ORR catalysts are often designed as a two-component catalyst system, combining the ORR catalysts such as Fe–N–C with highly active OER catalysts such as NiFe layered double hydroxides (LDH).<sup>[115]</sup> Although NiFeO<sub>x</sub> has been used for over a century as, *e.g.*, the OER catalyst in electrolyzers, the question of its active centers has not yet been fully clarified. Nickel alone is relatively inactive, however, it gains significantly when iron is intercalated into the structure. There are numerous studies which claimed to identify nickel<sup>[116,117]</sup> or iron<sup>[118,119]</sup> as the active sites. In addition, it is an open question whether only the surface of a NiFeO<sub>x</sub> catalyst or also the bulk contributes to the reaction. Several studies indicate that not just the outer surface but also the bulk of the catalyst is active,<sup>[120,121]</sup> while others demonstrate that the TOFs of NiFeO<sub>x</sub> tend to decrease with higher loadings.<sup>[122]</sup>

The question, whether the bulk or only the surface of the NiFeO<sub>x</sub> catalyst contributes to the reaction was recently investigated by C. Roy and co-workers.<sup>[123]</sup> Size-selected nanoparticles were used, and the exchange of lattice oxygen was investigated by isotope labeling experiments. A magnetron sputtering nanoparticle source was utilized to produce monodisperse, size-selected, and chemically pure metallic NiFe particles. A TEM image of the particles with average sizes of 3.9 ± 0.5 nm, 5.4 ± 0.6 nm, 6.7 ± 0.5 nm, and 8.4 ± 0.5 nm is shown in Figure 10a. The nanoparticles with the smallest sizes of 3.9 nm showed the highest mass activity, as shown in Figure 10b. However, all clusters showed significant OER currents already at an overpotential of η = 270 mV. Electrochemical mass spectrometry (EC-MS) was utilized to investigate if subsurface and lattice oxygen participates in the OER. Therefore, the <sup>16</sup>O labeled catalyst samples were investigated in <sup>18</sup>O-labeled 0.1 M KOH. As can be seen in Figure 10c, the release of <sup>16</sup>O was only observed at potentials above the onset of the OER. The signal was calibrated to m/z = 34 (<sup>16</sup>O/<sup>18</sup>O). The purple,

cyan, and blue dashed lines are simulations of a theoretical signal that would be monitored if 1% of the total <sup>16</sup>O exchanged with the electrolyte at the open circuit potential (OCP) within 5 s, 15 s, and 45 s, respectively. These simulations were introduced to demonstrate that even small release rates can be tracked by the EC-MS setup. Before and after the EC-MS experiments low-energy ion scattering (LEIS) spectra were recorded to observe the total change of <sup>16</sup>O/<sup>18</sup>O ratio. Corresponding spectra of the as-deposited (grey line), after OER measurements (purple line), and of the catalyst after additional sputtering to remove residuals from the electrolyte (blue line) are shown in Figure 10d. As expected, the <sup>16</sup>O/<sup>18</sup>O ratio decreased after OER as <sup>16</sup>O was exchanged with <sup>18</sup>O. After sputtering, the <sup>16</sup>O/<sup>18</sup>O ratio slightly increased as residuals from the <sup>18</sup>O-labeled electrolyte were removed. Importantly, in any case, the <sup>16</sup>O signal was still significant. The authors assigned this to the oxygen in the bulk catalyst and concluded that this was not exchanged during the OER. As a control experiment, the authors also performed the same experiment with reverse labeled oxygen species and observed similar trends. With this study, C. Roy and co-workers gave strong experimental evidence against the bulk activity NiFeO<sub>x</sub> catalysts as lattice oxidation and oxidation of low-mobility intercalated water were not detected. Further, they found that the OER mechanism does not involve lattice oxygen.<sup>[123]</sup> The approach of isotope labeling to size-selected nanoparticles is exemplary and could be extended to other systems with an uncertain contribution of the bulk catalyst.

## 6. Impact of the Supporting Electrolyte Components on the Active Site Performance

Up until now, we have discussed the activity of different catalyst materials, including the structure-activity relations and the concept of active sites. In addition to the composition and

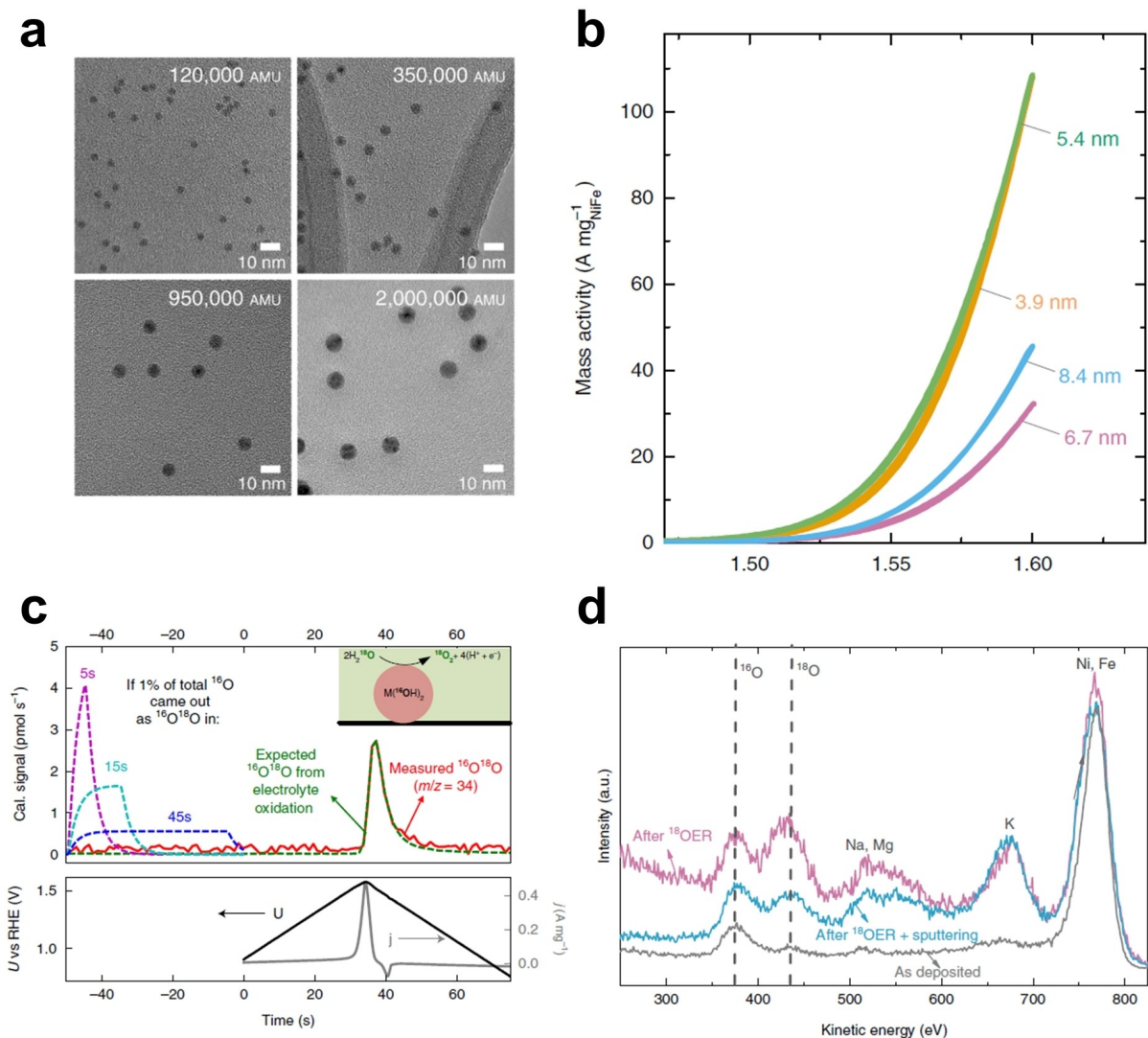


**Figure 10.** Size-selected NiFe nanoparticles. **a)** Representative TEM images of the nanoparticles with size of  $3.9 \pm 0.5$  nm,  $5.4 \pm 0.6$  nm,  $6.7 \pm 0.5$  nm, and  $8.4 \pm 0.5$  nm. **b)** Measurement of their OER activity in 1 M KOH. Currents are normalized to mass. **c)** EC-MS of  $\text{Ni}_x\text{Fe}_{1-x}(\text{OH})_2$  measured in  $^{18}\text{O}$ -labelled 0.1 M KOH during OER (red line). The green line shows the expected signal for the assumption that no lattice oxygen is exchanged. The purple, cyan, and blue dashed lines are simulations of a theoretical signal that would be monitored if 1% of total  $^{16}\text{O}$  exchanged with the electrolyte at OCP within 5 s, 15 s, and 45 s, respectively. **d)** LEIS spectra before (grey), after the OER (purple), and after additional sputtering (blue) to investigate  $^{16}\text{O}$  and  $^{18}\text{O}$  content. Reprinted with permission from Ref. [123]. Copyright (2018) Springer.

structure of the electrode material, in electrocatalysis, there is also a peculiar influence of the electrolyte species on the overall performance. There have been numerous studies describing how the nature of active sites changes in the presence of “inert” electrolyte species.<sup>[124–131]</sup> In this section, several of such important studies focusing on the ORR and OER electrocatalysis in different electrolytes are highlighted.

For a clear understanding of the influence of inert electrolyte species, one needs to limit the number of variables, which can be done by using model electrode systems. For this purpose, let us consider the influence of the electrolyte species on the Pt electrode, which is a well-known catalyst for the ORR. Alkali metal cations in the electrolyte have been shown to alter the activity of Pt surfaces significantly.<sup>[126–128]</sup> The proposed physical origin of this peculiar influence is thought to be

through so-called non-covalent interactions, where the alkali metal cations interact with oxygenated species adsorbed on the Pt surface (*i.e.*, Pt–OH). This mechanism is different from the specific adsorption and blocking of the active sites by anions in the electrolyte, for instance, blockage of the active sites on Pt by  $\text{HSO}_3^-/\text{SO}_3^{2-}$ .<sup>[132]</sup>

The ORR activity of the Pt(111) surface, in 0.1 M MOH (*M*: alkali metals) solutions, changes linearly with the hydration energy of the alkali metal cations, and the activity decreases in the following order:  $\text{Cs}^+ > \text{K}^+ > \text{Na}^+ > \text{Li}^+$ .<sup>[126]</sup> However, the trend is more complex for stepped single crystalline surfaces (*i.e.* Pt(221), Pt(331)), where the activity decreases in the following order:  $\text{K}^+ > \text{Na}^+ > \text{Cs}^+ > \text{Rb}^+ \approx \text{Li}^+$ .<sup>[127]</sup> Figure 11a summarizes the ORR activity of Pt stepped single-crystalline electrodes in different alkaline solutions, including the activities in

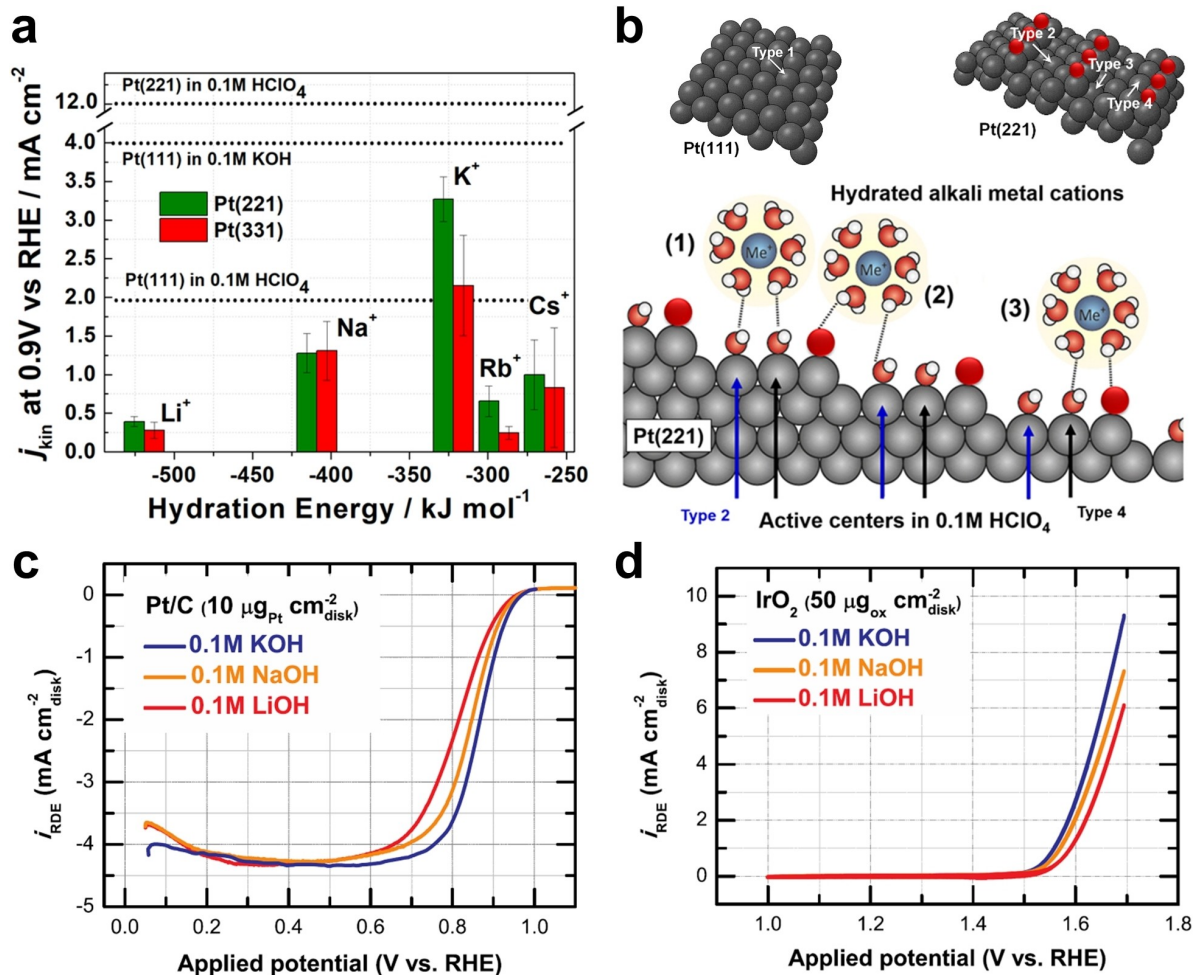


**Figure 11.** a) The ORR kinetic current densities for Pt(221) and Pt(331) electrodes in different 0.1 M alkali metal hydroxide solutions at the electrode potential 0.9 V. The ORR activities of Pt(111) in 0.1 M HClO<sub>4</sub>, 0.1 M KOH, and Pt(221) in 0.1 M HClO<sub>4</sub>, are shown by dotted lines for comparison. b) Schematic illustration of different surface catalytic sites on top of Pt(111) and Pt(221) electrodes. Red spheres represent the oxygen atoms, which permanently block the under-coordinated step-top sites on the surface of Pt(221). The lower image in (b) describes the non-covalent interaction between hydrated alkali metal cations with OH-adsorbates on terraces and steps of Pt(221). Red and white spheres represent oxygen and hydrogen, respectively. Blue-colored spheres represent alkali metal cations. Reprinted with permission from Ref. [127]. Copyright (2018) ACS. c) The polarization curves (anodic scan) of Pt/C in 0.1 M LiOH, NaOH, and KOH. d) The OER activity of r-IrO<sub>2</sub> in the same three alkaline solutions. Reprinted with permission from Ref. [135]. Copyright (2013) Springer.

acidic solutions for comparison. From these observations, it is clear that the nature of the active sites varies when the electrolyte composition is changed. Figure 11b illustrates the types of possible active sites on plain and stepped single-crystalline Pt surfaces. For a plain Pt(111) surface, one can assume that only one type (Type 1) of surface sites is present, and in acidic solution, they bind OH-intermediates *ca.* 0.1 eV stronger than the optimal value.<sup>[23,133]</sup> In alkaline solutions, the OH-binding energy is weakened due to the non-covalent interactions of alkali metal cations with the OH-adsorbates on the surface. Hence, the Pt(111) shows higher ORR activity in alkaline solutions in comparison to acidic. In addition, the degree of such non-covalent interaction is dependent on the nature and the hydration energy of the alkali metal cations.<sup>[126]</sup> For Pt(221) surfaces, one can assume to have four different surface sites, as illustrated in Figure 11b. Two of them are sacrificial surface sites: the first are permanently blocked "under-coordinated" sites located on the top edges (blocked by

red atoms as indicated in Figure 11b). The second sacrificial site, labeled Type 3, are sterically hindered. In acidic solution, the Type 2 sites of Pt(221) are the most active sites towards the ORR and demonstrate the most optimal OH-binding energy for the intermediates.<sup>[23]</sup> In alkaline solution, due to the influence of the alkali metal cations, the OH-binding strength will be shifted away from the near-optimal value and will lead to lower activities. In fact, lower ORR activities are observed in the basic solutions compared to the acidic ones (see Figure 11a). In alkaline solutions, the highest ORR activity for stepped Pt electrodes is observed in KOH. This finding was further experimentally confirmed by an *in-situ* EC-STM study, more information can be found in the Ref. [134].

Similar investigations have been done for Pt nanoparticles supported on carbon (Pt/C). The results are shown in Figure 11c.<sup>[135]</sup> The highest ORR activity for Pt/C is observed in the KOH solution. However, it should be noted that the authors did not perform the measurements in CsOH or RbOH. One can

translate the observations regarding the physical origins from the single crystalline electrode to nanostructured catalysts. Since the nanostructured materials will have various surface sites, including steps and terraces, similar to stepped single crystalline surfaces, one could expect analogous interactions between the alkali metal cations with the OH-adsorbates on the nanoparticle surface. In order to see if the alkali metal cations influence the OER activity, rutile (*r*)-IrO<sub>2</sub> nanoparticles have been investigated in different solutions. The results are given in Figure 11d. Similar to Pt/C, for IrO<sub>2</sub>, the highest OER activity is observed in KOH.

The influence of metal cations has also been investigated for transition metal-based electrocatalysts. The state-of-the-art transition metal-based OER catalyst in alkaline electrolytes is nickel oxyhydroxide (NiOOH) doped with Fe. The influence of electrolyte cations and anions has been extensively investigated for Fe doped and pure NiOOH.<sup>[136,137]</sup> Regarding the anions in the solution, the presence of most basic anions has shown to result in the highest OER activities for NiOOH. Among the alkali metal cations, the presence of Cs<sup>+</sup> yielded the highest OER activity, and the OER overpotential increased with decreasing ionic radii of the cations. The NiOOH based catalysts have a layered structure, and the species in the electrolyte (including water molecules) can intercalate between those catalyst layers.<sup>[138]</sup> The intercalation of water molecules and Na<sup>+</sup> cations in-between the NiOOH layers is schematically shown in Figure 12a. These intercalations can then alter the phase structure

of the catalyst leading to changes in their electrocatalytic performance. Figure 12b shows the activities of NiO<sub>x</sub>H<sub>y</sub> and Ni<sub>z-1</sub>Fe<sub>z</sub>O<sub>x</sub>H<sub>y</sub> (with 10% and 50% Fe doping) in different 0.1 M metal hydroxide solutions. A similar trend is observed for both Fe doped and pure NiO<sub>x</sub>H<sub>y</sub>. The overpotential at TOF of 0.1 s<sup>-1</sup> for NiO<sub>x</sub>H<sub>y</sub> in different basic solutions increased as follows: KOH ≈ NaOH ≈ Mg(OH)<sub>2</sub> << Ca(OH)<sub>2</sub>. For both 10% and 50% Fe doped samples of Ni(Fe)O<sub>x</sub>H<sub>y</sub>, a similar trend in the overpotential was observed: KOH ≈ Mg(OH)<sub>2</sub> < NaOH << Ca(OH)<sub>2</sub>.<sup>[138]</sup>

In summary, these studies show how the “inert” electrolyte species can alter the electrocatalytic performance of various materials. In addition, the differences in the physical origin of their influence on different catalyst materials are highlighted. For instance, depending on the electrode material, the electrolyte species can change the electrode activity through non-covalent interactions or through intercalations into the catalyst lattice. These aspects need to be carefully considered when designing electrocatalytic systems.<sup>[139]</sup>

## 7. In-situ Active Site Detection Techniques

To facilitate the design and increase the efficiency of bifunctional catalysts, it is of fundamental importance to understand which surface sites participate in the reaction. Maximizing the density of exposed active sites on the surface would lead to significantly improved catalytic performances.<sup>[80,140]</sup> Conse-

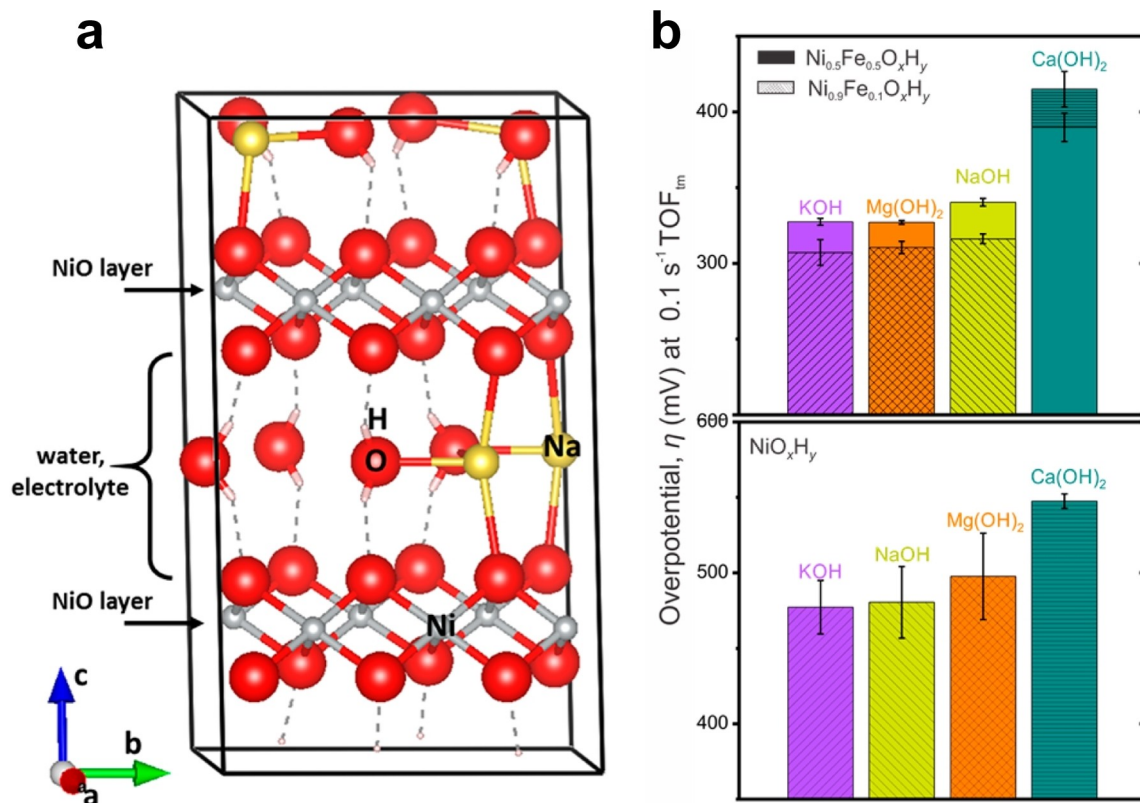


**Figure 12.** a) The schematics of a NiOOH crystal structure highlighting the intercalation of Na<sup>+</sup> and water molecules. b) The OER overpotential of NiO<sub>x</sub>H<sub>y</sub> and Ni<sub>z-1</sub>Fe<sub>z</sub>O<sub>x</sub>H<sub>y</sub> (with 10% and 50% Fe doping) in 0.1 M KOH, 0.1 M NaOH, 1 mM Ca(OH)<sub>2</sub> in 0.1 M KOH, and 1 mM Mg(OH)<sub>2</sub> in 0.1 M KOH. Reprinted with permission from Ref. [138]. Copyright (2017) ACS.

quently, it is desirable to observe the behavior of the catalyst surface under reaction conditions. Recently, specific experimental techniques have been developed that can identify the active sites under these circumstances. In the following, several techniques capable of *in-situ* detection of active surface structures will be presented.

A popular approach to probe the active sites of a surface is XAS.<sup>[66,141–146]</sup> Here, an X-ray photon beam, scanning through a range of energies, is directed at the sample (see Figure 13a). At specific energies, inner shell electrons are excited to a higher unoccupied energy level (Figure 13b). Consequently, the ratio

of the X-ray photons transmitted through the sample compared to the incident beam will yield information about the existing energy states. XAS spectra are typically divided in the extended XAFS (EXAFS) and the XANES, as indicated in Figure 13c. Especially the latter can be used for the identification of active electrocatalytic sites. The reason behind this is the slight modifications of the energy levels caused by adsorbed species. Peaks in the vicinity of an absorption edge give clues about the existing adsorbed species and combining them with electrochemical information of the sample can elucidate the active sites. An example of this is given in Figure 13d–f. Here, an N-

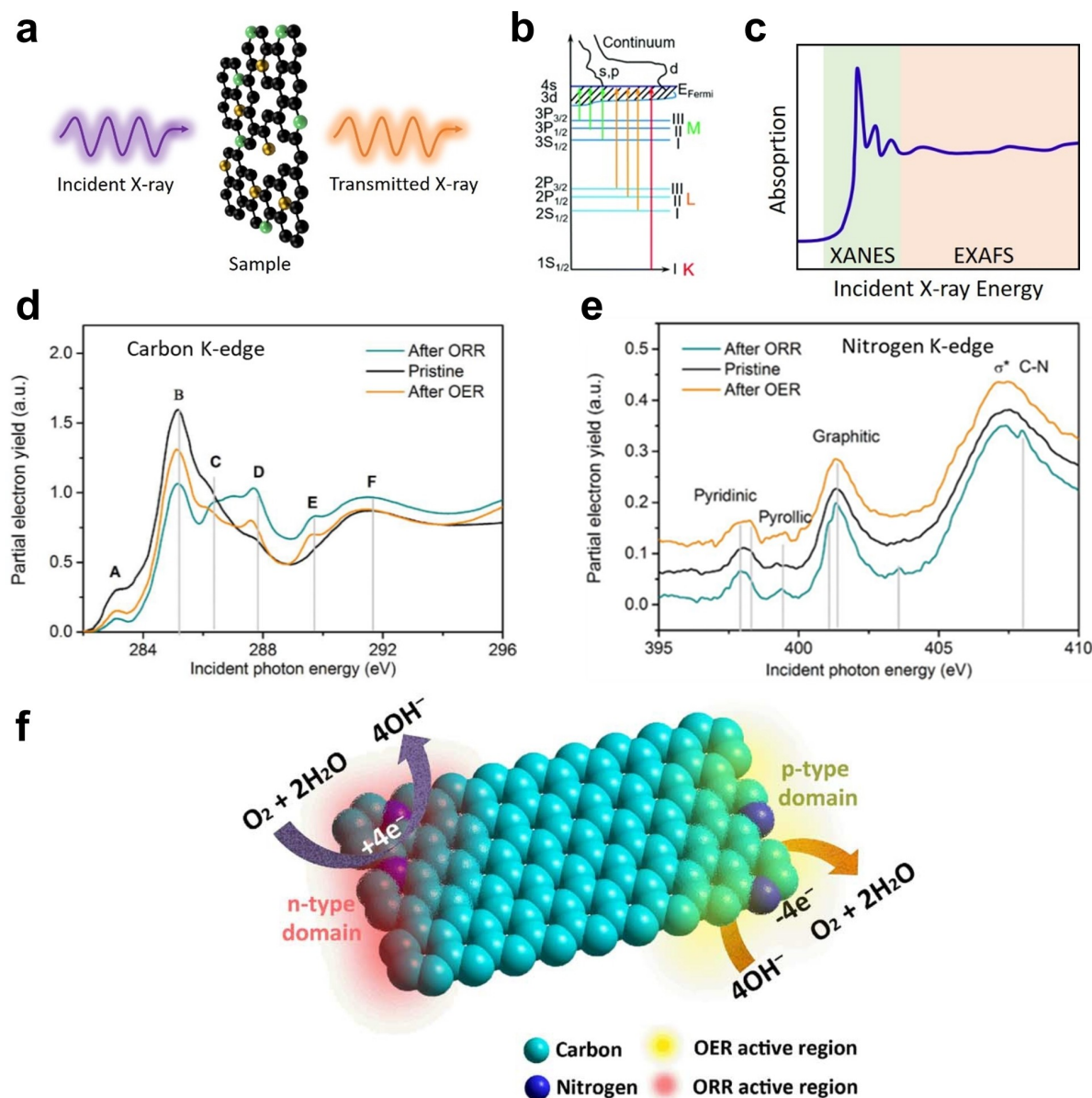


**Figure 13.** X-ray Absorption Near-Edge Spectra. **a**) In XAS, an X-ray beam is directed at the sample and scanned through a range of energies. The absorption ratio returns information about the chemical state of the sample. **b**) At specific energies, the incident beam will elevate inner shell electrons to the continuum level. Reproduced from Ref. [141] with permission from The Royal Society of Chemistry **c**) The XAS spectrum is divided into the EXAFS and XANES region. The latter reveals a shift in the electronic structure of the sample caused by adsorbed species. **d**) Carbon and **e**) nitrogen K-edge spectra of the pristine N-doped graphene catalyst, as well as after the ORR and after the OER. In **d**) A: defects, B:  $\pi^*_{C=C}$ , C:  $\pi^*_{C-OH}$ , D:  $\pi^*_{C-O-C, C-N}$ , E:  $\pi^*_{C=O, COOH}$ , F:  $\sigma^*_{C-C}$ . In **d**), the peaks D and E, corresponding to adsorbed  $^*O$  and  $^*OOH$  intermediates, grow after the reactions. In **e**), the growth of the graphitic peak after the ORR and the pyridinic peak after the OER elucidate their activity for the respective reaction. **f**) Following these results, the oxygen reduction occurs predominantly at n-type doped domains, whereas the OER is more likely to occur at the p-type domains. Reprinted with permission from Ref. [66]. Copyright (2016) AAAS.

doped graphene sample was investigated in an alkaline medium for the ORR and OER.<sup>[142]</sup> XANES spectra of the sample were measured under pristine conditions after going to the ORR and OER conditions. In this case, the XANES was measured under ultra-high vacuum (UHV). However, it is also possible to perform XANES *in-situ*.<sup>[141,143–145]</sup> Figure 13d shows the carbon K-edge of the sample; Figure 13e the nitrogen K-edge. The appearance of peaks at 287.7 eV and 289.6 eV in Figure 13d indicates adsorption of \*O and \*OOH reaction intermediates during both reactions. In Figure 13e, the new peak after ORR at 401 eV (slightly to the left of the graphitic peak) is presumably caused by lattice distortion due to \*O and \*OOH intermediates close to graphitic (quaternary) N. Combined with the observation that the pyridinic peak does not change after the reaction, the study suggests that the n-type doping (quaternary N) is the origin of ORR activity. On the other hand, after the OER, the pyridinic N peak at 398.0 eV in Figure 13e shows the largest growth compared to the pristine material, while the other peaks are largely unaffected. This leads to the assumption that the p-type doping (pyridinic N) is most active towards the OER. These results are summarized in Figure 13f, demonstrating the bifunctionality of the material.

Other approaches try to combine structural and activity information directly. An example of this is the SECCM.<sup>[147–153]</sup> The

idea is to miniaturize an electrochemical cell and use it as a scanning probe measuring the activity of a nanosized surface area. Scanning the probe over the surface at regular intervals and combining data returns an 'activity map' of the surface. The principle is illustrated in Figure 14a.<sup>[151]</sup> The scanning probe/electrochemical cell is comprised of a two-channel capillary (diameter < 500 nm), each containing the electrolyte and a quasi-reference counter electrode.<sup>[149]</sup> The ion current  $I_{IC}$  induced by an applied potential  $V_2$  between the two compartments, can be used for precise positioning in the z-direction. The potential  $V_1$  controls the voltage at the sample and, consequently, its electrochemical behavior. The probe is connected to the surface by an electrolyte meniscus. Upon contact with the surface, an electrochemical current  $I_{EC}$  is observed. Scanning the probe over the surface and monitoring this current returns an electrochemical map of the surface. In the example presented in Figure 14b, Unwin and co-workers demonstrate the technique for the ORR on a single-walled carbon nanotube (SWNT) on a Si/SiO<sub>2</sub> support.<sup>[151]</sup> An activity map of the SWNT under ORR conditions close to the reaction onset is shown. Considering the recorded current, the SWNT (up to -300 fA) can be readily distinguished from the inactive support material (close to 0fA) and confirms the expected electrochemical activity of this structure. In Figure 14c–e, the

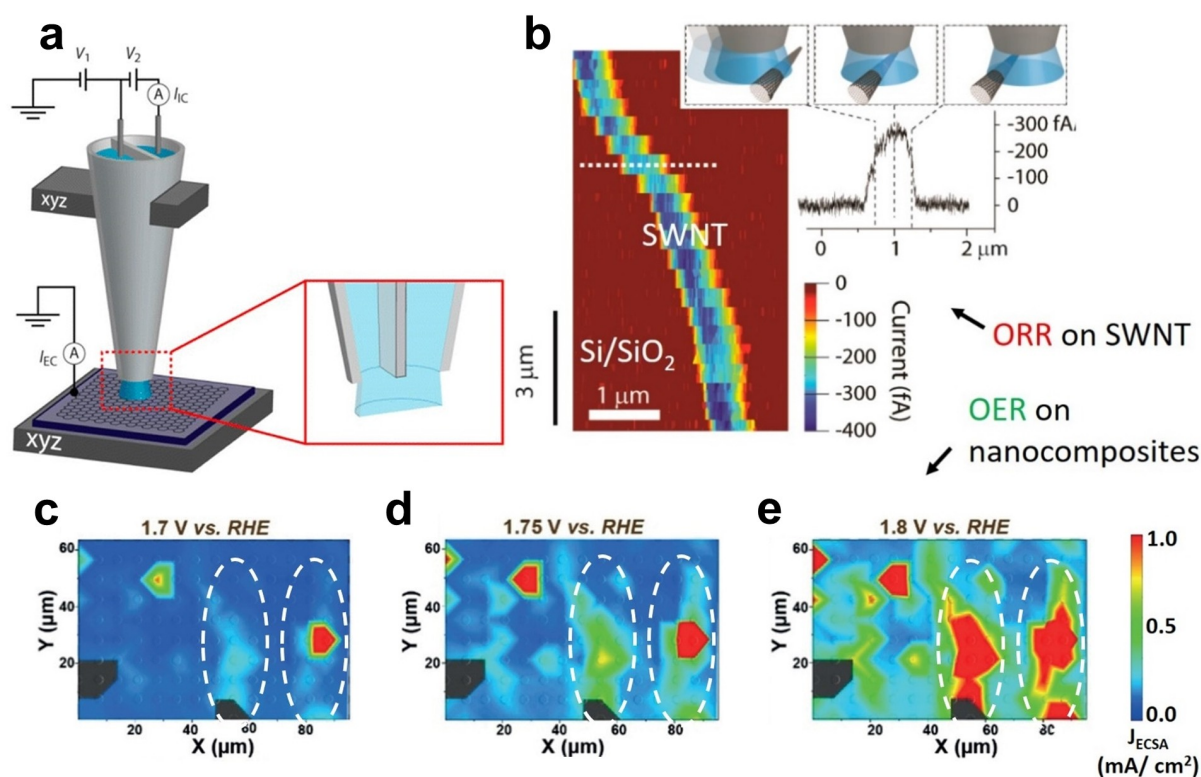


**Figure 14.** Scanning Electrochemical Cell Microscopy. **a)** The SECCM probe is a miniature electrochemical cell connected to the sample/working electrode by an electrolyte meniscus. The current  $I_{IC}$  is used for the z-positioning of the probe, while the electrochemical current  $I_{EC}$  reflects the local surface activity. Adapted with permission from [151]. Copyright (2016) ACS. **b)** In this example, the probe was moved over an SWNT on a Si/SiO<sub>2</sub> substrate under ORR conditions. The measurement reveals a uniform increase in current/activity at the SWNT compared to the substrate. Reprinted with permission from Ref. [152]. Copyright (2014) ACS. **c), d)** and **e)** show SECCM activity maps of Co-N/C nanocomposites on a GC support at several OER potentials (1.7, 1.75, and 1.8 vs. RHE respectively). Two areas of high nanoparticle densities are marked by the white dotted circles. With increasing potential, an increasing current density is observed, especially in these areas. Adapted with permission from Ref. [153]. Copyright (2019) Wiley.

principle is applied to Co–N/C nanocomposites under OER conditions (1.7 V, 1.75 V, and 1.8 V vs. RHE).<sup>[153]</sup> In this case, the probe was not continuously scanned over the surface. Instead, measurements were taken in intervals of 7  $\mu\text{m}$  in x- and y-directions. The spaces in between are extrapolated by the analysis software. The nanoparticles are on glassy carbon (GC) support and should therefore distinguish themselves by a higher OER activity in the SECCM measurement. Indeed, areas with a large nanoparticle density (encircled by a white dotted line) exhibit larger current density. Furthermore, with increasing potential, the activity of the nanoparticles increases as well.

These results show that SECCM is a versatile technique and readily applicable to determine the active areas on bifunctional electrocatalysts. The resolution of this technique is limited by the size of the meniscus connecting the scanning probe and sample.<sup>[147,149]</sup>

An additional technique to determine the position of active sites *in-situ* is noise analysis in electrochemical scanning tunneling microscopy (n-EC-STM).<sup>[24,51,134,154–157]</sup> Unlike the aforementioned techniques, the method benefits from the outstanding resolution of STM, and was proven to resolve the surface down to the atomic scale.<sup>[158]</sup> As a setup, a conventional STM is used in an electrochemical configuration, which allows detailed mapping of the surface morphology. The electrochemical compartment is comprised of a miniature electrochemical cell containing the sample, as well as a quasi-reference

and counter electrode. The tip is insulated against Faradaic reactions, *e.g.*, with wax, exposing only a few atoms to interact with the sample. The setup is connected to a bipotentiostat to regulate the tip and working electrode (sample) potentials. Consequently, the occurrence of reactions at the sample surface can be controlled. The STM signal (current or height) depends on the tunneling barrier between tip and sample. If the sample potential is set to a value that inhibits reactions, the tunneling barrier is stable at all places. Consequently, the STM image will yield a conductivity map of the surface, which implicitly reflects the surface morphology. Setting the sample potential to a value where a reaction is occurring will influence the tunneling barrier. The extent of this influence depends on the local electrochemical activity. Essentially, a reaction process continuously rearranges the electrolyte structure. However, this is locally confined to the active site. Therefore, if the tip is placed over an active site, this process occurs within the tunneling gap, which will change the tunneling barrier and consequently the tunneling current.<sup>[24,154,159–162]</sup> As a result, the STM signal over an active site is superimposed by noise originating from the electrochemical reaction, while the STM signal over non-active sites is noise-free. This principle is sketched in Figure 15a. Here, the active sites are indicated by orange arrows. The resulting STM profile (purple) shows that active sites can be identified by the noise spikes while the rest of the surface is traced with a stable, noise-free signal. In Figure 15b, the method is demon-

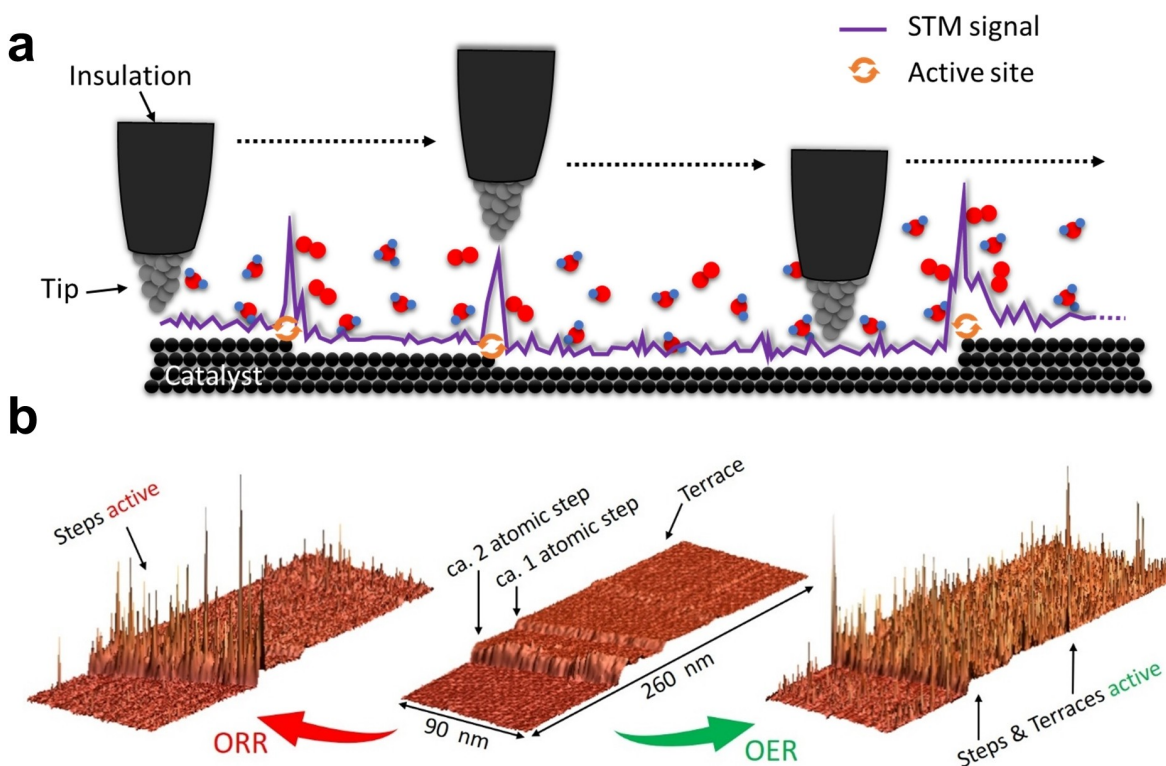


**Figure 15.** n-EC-STM measurements. **a)** Over non-active sites, the tunneling current is stable, and the STM signal (purple) will reflect the surface morphology. At active sites (marked by orange arrows), the continuous reaction process disturbs the tunneling barrier, which results in distinct noise spikes in the STM profile. **b)** The n-EC-STM technique can be used to determine bifunctionally active sites. Here, steps and terraces on HOPG are investigated in 0.1 M KOH for both ORR and OER. The resulting images suggest that the majority of activity for the ORR arises from step sites, whereas the activity for the OER is originating from steps as well as terraces. Adapted with permission from Ref. [51]. Copyright (2021) Elsevier.

strated for HOPG in an alkaline medium (0.1 M KOH) for ORR and OER.<sup>[51]</sup> We investigate a surface structure consisting of steps and terraces, which are clearly visible while the reactions are 'off' (middle in Figure 15b). Applying ORR conditions (left in Figure 15b) leads to large noise spikes along the steps, while the terraces are mostly inactive. Considering the research consensus on comparable systems expanded upon in section 2, one can assume that the intermittent activity on terraces originates from defective sites. At the same time, the pristine basal plane is inactive. For the OER (right in Figure 15b), on the other hand, the noise is distributed uniformly across the entire surface. This suggests an involvement of both basal and edge planes in the OER. However, the stability of the material under OER conditions is not clear. Moreover, although the study suggests commensurate stability at lower current densities, the consequences of higher current densities are not fully understood yet.

Besides the techniques highlighted in this section, there are further experimental methods capable of detecting catalytic activity, such as scanning electrochemical microscopy (SECM), electrochemical tip-enhanced Raman spectroscopy (EC-TERS), and crystal truncation rod analysis (CTR).<sup>[163–165]</sup> All of the methods possess individual advantages and shortcomings. Consequently, it is important to premeditate the requirements of the electrocatalytic system under investigation and select the experimental technique accordingly. This is especially relevant for the evaluation of bifunctional systems due to the many processes and species involved in the reactions. Moreover, although all of the presented techniques can readily identify active sites, it should always be considered whether theoretical approaches could be performed to support and strengthen the results.

## 8. Summary

The development of efficient electrocatalytic systems is a promising, sustainable solution to the ever-growing energy demands. The optimization of such electrochemical energy conversion devices largely depends on our understanding of the nature of the active sites. In this review, several of the most promising bifunctional electrocatalyst materials for the ORR and OER have been highlighted. Model systems are used to draw valuable conclusions from the experiments. In this regard, thin films or extended single crystal surfaces can assist in the identification of the active centers. For instance, the structure-sensitivity relation can be traced back to surface orientation (as for rutile IrO<sub>2</sub> and RuO<sub>2</sub> thin films), material composition (as for perovskite structures with varying substitution of the constituent atoms), and to structural features (such as defect sites on carbon-based catalysts). MOFs and MOF derivatives offer a wider variety of options for the design of highly active bifunctional oxygen electrocatalysts, especially developing M–N–C active sites by precisely regulating the structure and composition of pristine MOFs at the molecular scale. Accordingly, these in-depth researches on MOF-based catalysts accelerated the understanding of the electrocatalytic active

centers and catalytic mechanism. Moreover, methods allowing for the investigation of individual entities with defined shapes and sizes are discussed. The obtained information can aid in understanding the electrochemistry at the nanoscale and improve catalytic properties under reaction conditions. Model extended surfaces have been used in elucidating how the "inert" species in the electrolyte can alter the electrode's activity. For instance, the physical origins behind the influence of certain metal cations on the performance of noble- and transition metal-based catalysts are elaborated. In addition, the instruments and techniques utilized in the determination of the active sites are described. Here, the emphasis is placed upon cutting-edge experimental approaches that can be utilized under reaction conditions, offer a high spatial resolution, and possess the versatility to investigate various classes of samples and reactions. Recent and upcoming advancements in the development of efficient bifunctional catalysts towards the ORR and OER will pave the way for large-scale applications of renewable energy conversion systems such as metal-air batteries, fuel cells, and electrolyzers.

## Acknowledgements

We are grateful for the financial support from Deutsche Forschungsgemeinschaft under Germany's excellence strategy – EXC 2089/1 – 390776260, Germany's excellence cluster "e-conversion", DFG project BA 5795/4-1 and BA 5795/5-1. We acknowledge the funding provided from the European Union's Horizon 2020 research and innovation program under grant agreement HERMES No 952184. Open access funding enabled and organized by Projekt DEAL.

## Conflict of Interest

The authors declare no conflict of interest.

**Keywords:** active sites · bifunctional electrocatalysts · electrocatalysis · oxygen evolution reaction · oxygen reduction reaction

- [1] H. S. Taylor, E. F. Armstrong, *Proc. R. Soc. London Ser. A* **1925**, *108*, 105–111.
- [2] J. Rossmeisl, Z.-W. Qu, H. Zhu, G.-J. Kroeis, J. K. Nørskov, *J. Electroanal. Chem.* **2007**, *607*, 83–89.
- [3] K. Zeng, D. Zhang, *Prog. Energy Combust. Sci.* **2010**, *36*, 307–326.
- [4] J. Quílez-Bermejo, E. Morallon, D. Cazorla-Amoros, *Carbon* **2020**, *165*, 434–454.
- [5] Q. Liang, G. Brocks, A. Bieberle-Hütter, *J. Phys. Energy* **2021**, *3*, 026001.
- [6] R. Ma, G. Lin, Y. Zhou, Q. Liu, T. Zhang, G. Shan, M. Yang, J. Wang, *NPJ Comput. Mater.* **2019**, *5*, 78.
- [7] D. Liu, Y. Tong, X. Yan, J. Liang, S. X. Dou, *Batteries & Supercaps* **2019**, *2*, 743–765.
- [8] G. Chen, J. Zhang, F. Wang, L. Wang, Z. Liao, E. Zschech, K. Müllen, X. Feng, *Chem. Eur. J.* **2018**, *24*, 18413–18418.
- [9] Y. Lian, W. Yang, C. Zhang, H. Sun, Z. Deng, W. Xu, L. Song, Z. Ouyang, Z. Wang, J. Guo, Y. Peng, *Angew. Chem. Int. Ed.* **2020**, *59*, 286–294; *Angew. Chem.* **2020**, *132*, 292–300.

- [10] S. S. Shinde, C. H. Lee, J.-Y. Jung, N. K. Wagh, S.-H. Kim, D.-H. Kim, C. Lin, S. U. Lee, J.-H. Lee, *Energy Environ. Sci.* **2019**, *12*, 727–738.
- [11] Y. Jia, L. Zhang, A. Du, G. Gao, J. Chen, X. Yan, C. L. Brown, X. Yao, *Adv. Mater.* **2016**, *28*, 9532–9538.
- [12] M. Wang, W. Wang, T. Qian, S. Liu, Y. Li, Z. Hou, J. B. Goodenough, P. M. Ajayan, C. Yan, *Adv. Mater.* **2019**, *31*, 1803339.
- [13] S. S. Shinde, C. H. Lee, J.-Y. Yu, D.-H. Kim, S. U. Lee, J.-H. Lee, *ACS Nano* **2018**, *12*, 596–608.
- [14] X. Duan, S. Ren, N. Pan, M. Zhang, H. Zheng, *J. Mater. Chem. A* **2020**, *8*, 9355–9363.
- [15] T. Wang, Z. Kou, S. Mu, J. Liu, D. He, I. S. Amiinu, W. Meng, K. Zhou, Z. Luo, S. Chaemchuen, F. Verpoort, *Adv. Funct. Mater.* **2018**, *28*, 1705048.
- [16] S. Liu, M. Wang, X. Sun, N. Xu, J. Liu, Y. Wang, T. Qian, C. Yan, *Adv. Mater.* **2018**, *30*, 1704898.
- [17] M. Wang, T. Qian, J. Zhou, C. Yan, *ACS Appl. Mater. Interfaces* **2017**, *9*, 5213–5221.
- [18] Q. Wang, Y. Lei, Z. Chen, N. Wu, Y. Wang, B. Wang, Y. Wang, *J. Mater. Chem. A* **2018**, *6*, 516–526.
- [19] B. Chen, X. He, F. Yin, H. Wang, D.-J. Liu, R. Shi, J. Chen, H. Yin, *Adv. Funct. Mater.* **2017**, *27*, 1700795.
- [20] C.-C. Weng, J.-T. Ren, Z.-P. Hu, Z.-Y. Yuan, *ACS Sustainable Chem. Eng.* **2018**, *6*, 15811–15821.
- [21] S. Liu, X. Zhang, G. Wang, Y. Zhang, H. Zhang, *ACS Appl. Mater. Interfaces* **2017**, *9*, 34269–34278.
- [22] C. Guan, A. Sumbaja, H. Wu, W. Ren, X. Liu, H. Zhang, Z. Liu, C. Cheng, S. J. Pennycook, J. Wang, *Adv. Mater.* **2017**, *29*, 1704117.
- [23] F. Calle-Vallejo, M. D. Pohl, D. Reinisch, D. Loffreda, P. Sautet, A. S. Bandarenka, *Chem. Sci.* **2017**, *8*, 2283–2289.
- [24] R. W. Haid, R. M. Kluge, Y. Liang, A. S. Bandarenka, *Small Methods* **2021**, *5*, 2000710.
- [25] K. A. Stoerzinger, L. Qiao, M. D. Biegalski, Y. Shao-Horn, *J. Phys. Chem. Lett.* **2014**, *5*, 1636–1641.
- [26] S. Cherevko, S. Geiger, O. Kasian, N. Kulyk, J.-P. Grote, A. Savan, B. R. Shrestha, S. Merzlikin, B. Breitbach, A. Ludwig, K. J. J. Mayrhofer, *Catal. Today* **2016**, *262*, 170–180.
- [27] Y. Gorlin, B. Lassalle-Kaiser, J. D. Benck, S. Gul, S. M. Webb, V. K. Yachandra, J. Yano, T. F. Jaramillo, *J. Am. Chem. Soc.* **2013**, *135*, 8525–8534.
- [28] T. Reier, M. Oezaslan, P. Strasser, *ACS Catal.* **2012**, *2*, 1765–1772.
- [29] J. Prakash, H. Joachin, *Electrochim. Acta* **2000**, *45*, 2289–2296.
- [30] O. Diaz-Morales, S. Raaijman, R. Kortlever, P. J. Kooyman, T. Wezendonk, J. Gascon, W. T. Fu, M. T. M. Koper, *Nat. Commun.* **2016**, *7*, 12363.
- [31] J. R. Petrie, V. R. Cooper, J. W. Freeland, T. L. Meyer, Z. Zhang, D. A. Lutterman, H. N. Lee, *J. Am. Chem. Soc.* **2016**, *138*, 2488–2491.
- [32] J. R. Petrie, H. Jeen, S. C. Barron, T. L. Meyer, H. N. Lee, *J. Am. Chem. Soc.* **2016**, *138*, 7252–7255.
- [33] C. Wei, Z. Feng, G. G. Scherer, J. Barber, Y. Shao-Horn, Z. J. Xu, *Adv. Mater.* **2017**, *29*, 1606800.
- [34] M. A. Green, A. Ho-Baillie, H. J. Snaith, *Nat. Photonics* **2014**, *8*, 506–514.
- [35] D. Zhang, Y. Song, Z. Du, L. Wang, Y. Li, J. B. Goodenough, *J. Mater. Chem. A* **2015**, *3*, 9421–9426.
- [36] L. Wang, K. A. Stoerzinger, L. Chang, J. Zhao, Y. Li, C. S. Tang, X. Yin, M. E. Bowden, Z. Yang, H. Guo, R. Guo, J.-O. Wang, K. Ibrahim, J. Chen, A. Rusydi, J. Wang, S. A. Chambers, Y. Du, *Adv. Funct. Mater.* **2018**, *28*, 1803712.
- [37] J. Sunarso, A. A. J. Torriero, W. Zhou, P. C. Howlett, M. Forsyth, *J. Phys. Chem. C* **2012**, *116*, 5827–5834.
- [38] J. Suntivich, H. A. Gasteiger, N. Yabuuchi, H. Nakanishi, J. B. Goodenough, Y. Shao-Horn, *Nat. Chem.* **2011**, *3*, 546–550.
- [39] J. Suntivich, K. J. May, H. A. Gasteiger, J. B. Goodenough, Y. Shao-Horn, *Science* **2011**, *334*, 1383–1385.
- [40] M. Risch, K. A. Stoerzinger, S. Maruyama, W. T. Hong, I. Takeuchi, Y. Shao-Horn, *J. Am. Chem. Soc.* **2014**, *136*, 5229–5232.
- [41] S. H. Chang, N. Danilovic, K. C. Chang, R. Subbaraman, A. P. Paulikas, D. D. Fong, M. J. Highland, P. M. Baldo, V. R. Stamenkovic, J. W. Freeland, J. A. Eastman, N. M. Markovic, *Nat. Commun.* **2014**, *5*, 4191–4200.
- [42] A. Ambrosi, C. K. Chua, N. M. Latiff, A. H. Loo, C. H. an Wong, A. Y. S. Eng, A. Bonanni, M. Pumer, *Chem. Soc. Rev.* **2016**, *45*, 2458–2493.
- [43] D. A. C. Brownson, D. K. Kampouris, C. E. Banks, *Chem. Soc. Rev.* **2012**, *41*, 6944–6976.
- [44] S. Maldonado, K. J. Stevenson, *J. Phys. Chem. B* **2005**, *109*, 4707–4716.
- [45] E. Yeager, *Electrochim. Acta* **1984**, *29*, 1527–1537.
- [46] L. Zhang, Q. Xu, J. Niu, Z. Xia, *Phys. Chem. Chem. Phys.* **2015**, *17*, 16733–16743.
- [47] L. Tao, Q. Wang, S. Dou, Z. Ma, J. Huo, S. Wang, L. Dai, *Chem. Commun.* **2016**, *52*, 2764–2767.
- [48] A. Shen, Y. Zou, Q. Wang, R. A. W. Dryfe, X. Huang, S. Dou, L. Dai, S. Wang, *Angew. Chem. Int. Ed.* **2014**, *53*, 10804–10808; *Angew. Chem.* **2014**, *126*, 10980–10984.
- [49] Y. Jiang, L. Yang, T. Sun, J. Zhao, Z. Lyu, O. Zhuo, X. Wang, Q. Wu, J. Ma, Z. Hu, *ACS Catal.* **2015**, *5*, 6707–6712.
- [50] C. Tang, Q. Zhang, *Adv. Mater.* **2017**, *29*, 1604103.
- [51] R. W. Haid, R. M. Kluge, T. O. Schmidt, A. S. Bandarenka, *Electrochim. Acta* **2021**, *382*, 138285.
- [52] J. Sun, S. E. Lowe, L. Zhang, Y. Wang, K. Pang, Y. Wang, Y. Zhong, P. Liu, K. Zhao, Z. Tang, H. Zhao, *Angew. Chem. Int. Ed.* **2018**, *57*, 16511–16515; *Angew. Chem.* **2018**, *130*, 16749–16753.
- [53] Y. Lin, Q. Lu, F. Song, L. Yu, A. K. Mechler, R. Schlögl, S. Heumann, *Angew. Chem. Int. Ed.* **2019**, *58*, 8917–8921; *Angew. Chem.* **2019**, *131*, 9010–9014.
- [54] K. Qu, Y. Zheng, S. Dai, S. Z. Qiao, *Nano Energy* **2016**, *19*, 373–381.
- [55] G.-L. Tian, M.-Q. Zhao, D. Yu, X.-Y. Kong, J.-Q. Huang, Q. Zhang, F. Wei, *Small* **2014**, *10*, 2251–2259.
- [56] J.-C. Li, P.-X. Hou, S.-Y. Zhao, C. Liu, D.-M. Tang, M. Cheng, F. Zhang, H.-M. Cheng, *Energy Environ. Sci.* **2016**, *9*, 3079–3084.
- [57] S. Patra, R. Choudhary, E. Roy, R. Madhuri, P. K. Sharma, *Nano Energy* **2016**, *30*, 118–129.
- [58] L. Yang, S. Jiang, Y. Zhao, L. Zhu, S. Chen, X. Wang, Q. Wu, J. Ma, Y. Ma, Z. Hu, *Angew. Chem. Int. Ed.* **2011**, *50*, 7132–7135; *Angew. Chem.* **2011**, *123*, 7270–7273.
- [59] X. Kong, Q. Chen, Z. Sun, *ChemPhysChem* **2013**, *14*, 514–519.
- [60] S. Pylypenko, A. Queen, T. S. Olson, A. Dameron, K. O'Neill, K. C. Neyerlin, B. Pivovar, H. N. Dinh, D. S. Ginley, T. Gennett, R. O'Hayre, *J. Phys. Chem. C* **2011**, *115*, 13667–13675.
- [61] L. Qu, Y. Liu, J.-B. Baek, L. Dai, *ACS Nano* **2010**, *4*, 1321–1326.
- [62] L. Lai, J. R. Potts, Da. Zhan, L. Wang, C. K. Poh, C. Tang, H. Gong, Z. Shen, J. Lin, R. S. Ruoff, *Energy Environ. Sci.* **2012**, *5*, 7936–7942.
- [63] J. Masa, W. Xia, M. Muhler, W. Schuhmann, *Angew. Chem. Int. Ed.* **2015**, *54*, 10102.
- [64] D. W. Chang, H.-J. Choi, J.-B. Baek, *J. Mater. Chem. A* **2015**, *3*, 7659–7665.
- [65] J. Wu, L. Ma, R. M. Yadav, Y. Yang, X. Zhang, R. Vajtai, J. Lou, P. M. Ajayan, *ACS Appl. Mater. Interfaces* **2015**, *7*, 14763–14769.
- [66] H. B. Yang, J. Miao, S.-F. Hung, J. Chen, H. B. Tao, X. Wang, L. Zhang, R. Chen, J. Gao, H. M. Chen, L. Dai, B. Liu, *Sci. Adv.* **2016**, *2*, e1501122.
- [67] J. Maruyama, S. Maruyama, T. Fukuhara, H. Mizuhata, S. Takenaka, A. Yoshida, K. Miyazaki, *J. Electrochem. Soc.* **2020**, *167*, 060504.
- [68] Z.-F. Huang, J. Wang, Y. Peng, C.-Y. Jung, A. Fisher, X. Wang, *Adv. Energy Mater.* **2017**, *7*, 1700544.
- [69] J. Lee, O. K. Farha, J. Roberts, K. A. Scheidt, S. T. Nguyen, J. T. Hupp, *Chem. Soc. Rev.* **2009**, *38*, 1450.
- [70] Q.-L. Zhu, Q. Xu, *Chem. Soc. Rev.* **2014**, *43*, 5468–5512.
- [71] S. Hou, X. Xu, M. Wang, Y. Xu, T. Lu, Y. Yao, L. Pan, *J. Mater. Chem. A* **2017**, *5*, 19054–19061.
- [72] B. Y. Xia, Y. Yan, N. Li, H. B. Wu, X. W. Lou, X. Wang, *Nat. Energy* **2016**, *1*, 15006.
- [73] A. Bétard, R. A. Fischer, *Chem. Rev.* **2012**, *112*, 1055–1083.
- [74] J. Wu, H. Zhou, Q. Li, M. Chen, J. Wan, N. Zhang, L. Xiong, S. Li, B. Y. Xia, G. Feng, M. Liu, L. Huang, *Adv. Energy Mater.* **2019**, *9*, 1900149.
- [75] I. S. Amiinu, Z. Pu, X. Liu, K. A. Owusu, H. G. R. Monestel, F. O. Boakye, H. Zhang, S. Mu, *Adv. Funct. Mater.* **2017**, *27*, 1702300.
- [76] M. Zhang, Q. Dai, H. Zheng, M. Chen, L. Dai, *Adv. Mater.* **2018**, *30*, 1705431.
- [77] D. Sheberla, J. C. Bachman, J. S. Elias, C.-J. Sun, Y. Shao-Horn, M. Dincă, *Nat. Mater.* **2016**, *16*, 220–224.
- [78] M. Yang, X. Hu, Z. Fang, L. Sun, Z. Yuan, S. Wang, W. Hong, X. Chen, D. Yu, *Adv. Funct. Mater.* **2017**, *27*, 1701971.
- [79] C. Xuan, B. Hou, W. Xia, Z. Peng, T. Shen, H. L. Xin, G. Zhang, D. Wang, *J. Mater. Chem. A* **2018**, *6*, 10731–10739.
- [80] W. Li, S. Xue, S. Watzel, S. Hou, J. Fichtner, A. L. Semrau, L. Zhou, A. Welle, A. S. Bandarenka, R. A. Fischer, *Angew. Chem. Int. Ed.* **2020**, *59*, 5837–5843; *Angew. Chem.* **2020**, *132*, 5886–5892.
- [81] B. Garlyyev, J. Fichtner, O. Piqué, O. Schneider, A. S. Bandarenka, F. Calle-Vallejo, *Chem. Sci.* **2019**, *10*, 8060–8075.
- [82] D. Cheng, Z.-J. Zhao, G. Zhang, P. Yang, L. Li, H. Gao, S. Liu, X. Chang, S. Chen, T. Wang, G. A. Ozin, Z. Liu, J. Gong, *Nat. Commun.* **2021**, *12*, 395.
- [83] X. Xu, J. Tang, Y. V. Kaneti, H. Tan, T. Chen, L. Pan, T. Yang, Y. Bando, Y. Yamauchi, *Mater. Horiz.* **2020**, *7*, 1404–1412.

- [84] Y.-N. Chen, Y. Guo, H. Cui, Z. Xie, X. Zhang, J. Wei, Z. Zhou, *J. Mater. Chem. A* **2018**, *6*, 9716–9722.
- [85] B. Zhu, D. Xia, R. Zou, *Coord. Chem. Rev.* **2018**, *376*, 430–448.
- [86] A. Zitolo, N. Ranjbar-Sahraie, T. Mineva, J. Li, Q. Jia, S. Stamatini, G. F. Harrington, S. M. Lyth, P. Krtil, S. Mukerjee, E. Fonda, F. Jaouen, *Nat. Commun.* **2017**, *8*, 957.
- [87] M. Sun, D. Davenport, H. Liu, J. Qu, M. Elimelech, J. Li, *J. Mater. Chem. A* **2018**, *6*, 2527–2539.
- [88] P. Deria, J. E. Mondloch, O. Karagiari, W. Bury, J. T. Hupp, O. K. Farha, *Chem. Soc. Rev.* **2014**, *43*, 5896–5912.
- [89] B. Garlyyev, K. Kratzl, M. Rück, J. Michalička, J. Fichtner, J. M. Macak, T. Kratky, S. Günther, M. Cokoja, A. S. Bandarenka, A. Gagliardi, R. A. Fischer, *Angew. Chem. Int. Ed.* **2019**, *58*, 9596–9600; *Angew. Chem.* **2019**, *131*, 9697–9702.
- [90] P. Yu, L. Wang, F. Sun, Y. Xie, X. Liu, J. Ma, X. Wang, C. Tian, J. Li, H. Fu, *Adv. Mater.* **2019**, *31*, 1901666.
- [91] A. S. Varela, W. Ju, P. Strasser, *Adv. Energy Mater.* **2018**, *8*, 1703614.
- [92] Y. Chen, S. Ji, S. Zhao, W. Chen, J. Dong, W.-C. Cheong, R. Shen, X. Wen, L. Zheng, A. I. Rykov, S. Cai, H. Tang, Z. Zhuang, C. Chen, Q. Peng, D. Wang, Y. Li, *Nat. Commun.* **2018**, *9*, 5422.
- [93] E. M. Miner, T. Fukushima, D. Sheberla, L. Sun, Y. Surendranath, M. Dincă, *Nat. Commun.* **2016**, *7*, 10942.
- [94] W. Cheng, X. Zhao, H. Su, F. Tang, W. Che, H. Zhang, Q. Liu, *Nat. Energy* **2019**, *4*, 115–122.
- [95] X. Li, Y. Fang, X. Lin, M. Tian, X. An, Y. Fu, R. Li, J. Jin, J. Ma, *J. Mater. Chem. A* **2015**, *3*, 17392–17402.
- [96] L. Ma, S. Chen, Z. Pei, Y. Huang, G. Liang, F. Mo, Q. Yang, J. Su, Y. Gao, J. A. Zapien, C. Zhi, *ACS Nano* **2018**, *12*, 1949–1958.
- [97] S.-D. Yim, W.-Y. Lee, Y.-G. Yoon, Y.-J. Sohn, G.-G. Park, T.-H. Yang, C.-S. Kim, *Electrochim. Acta* **2004**, *50*, 713–718.
- [98] E. Antolini, *ACS Catal.* **2014**, *4*, 5, 1426–1440.
- [99] H. Osgood, S. V. Devaguptapu, H. Xu, J. Cho, G. Wu, *Nano Today* **2016**, *11*, 5, 601–625.
- [100] Y. Zhu, X. Liu, S. Jin, H. Chen, W. Lee, M. Liu, Y. Chen, *J. Mater. Chem. A* **2019**, *7*, 5875–5897.
- [101] C. M. Hill, J. Kim, A. J. Bard, *J. Am. Chem. Soc.* **2015**, *137*, 11321–11326.
- [102] Y. Yu, Y. Gao, K. Hu, P.-Y. Blanchard, J.-M. Noël, T. Nareshkumar, K. L. Phani, G. Friedmann, Y. Gogotsi, M. Mirkin, *ChemElectroChem* **2015**, *2*, 58–63.
- [103] B. M. Quinn, P. G. van't Hof, S. G. Lemay, *J. Am. Chem. Soc.* **2004**, *126*, 27, 8360–8361.
- [104] S. E. Kleijn, S. C. S. Lai, T. S. Miller, A. I. Yanson, M. T. M. Koper, P. R. Unwin, *J. Am. Chem. Soc.* **2012**, *134*, 18558–18561.
- [105] S. Chen, A. Kucernak, *J. Phys. Chem. B* **2004**, *108*, 3262–3276.
- [106] J. Clausmeyer, J. Masa, E. Ventosa, D. Öhl, W. Schuhmann, *Chem. Commun.* **2016**, *52*, 2408–2411.
- [107] J. Masa, C. Andronesco, W. Schuhmann, *Angew. Chem. Int. Ed.* **2020**, *59*, 15298–15312; *Angew. Chem.* **2020**, *132*, 15410–15426.
- [108] T. Quast, H. B. Aiyappa, S. Saddeler, P. Wilde, Y.-T. Chen, S. Schulz, W. Schuhmann, *Angew. Chem. Int. Ed.* **2021**, *60*, 3576–3580; *Angew. Chem.* **2021**, *133*, 3619–3624.
- [109] S. Saddeler, U. Hagemann, S. Schulz, *Inorg. Chem.* **2020**, *59*, 14, 10013–10024.
- [110] J. Kim, B.-K. Kim, S. K. Cho, A. J. Bard, *J. Am. Chem. Soc.* **2014**, *136*, 8173–8176.
- [111] J. H. Park, A. Boika, H. S. Park, H. C. Lee, A. J. Bard, *J. Phys. Chem. C* **2013**, *117*, 6651–6657.
- [112] C.-H. Chen, E. R. Ravenhill, D. Momotenko, Y.-R. Kim, S. C. S. Lai, P. R. Unwin, *Langmuir* **2015**, *31*, 11932–11942.
- [113] M. Kang, D. Perry, Y.-R. Kim, A. W. Colburn, R. A. Lazenby, P. R. Unwin, *J. Am. Chem. Soc.* **2015**, *137*, 34, 10902–10905.
- [114] G. Kwon, G. A. Ferguson, C. J. Heard, E. C. Tyo, C. Yin, J. DeBartolo, S. Seifert, R. E. Winans, A. J. Kropf, J. Greeley, R. L. Johnston, L. A. Curtiss, M. J. Pellin, S. Vajda, *ACS Nano* **2013**, *7*, 5808–5817.
- [115] S. Dresch, F. Luo, R. Schmack, S. Kühl, M. Glied, P. Strasser, *Energy Environ. Sci.* **2016**, *9*, 2020–2024.
- [116] M. Görlin, P. Chervin, J. Ferreira de Araújo, T. Reier, S. Dresch, B. Paul, R. Krähnert, H. Dau, P. Strasser, *J. Am. Chem. Soc.* **2016**, *138*, 5603–5614.
- [117] N. Li, D. K. Bediako, R. G. Hadt, D. Hayes, T. J. Kempa, F. von Cube, D. C. Bell, L. X. Chen, D. G. Nocera, *Proc. Natl. Acad. Sci. USA* **2017**, *114*, 1486–1491.
- [118] M. B. Stevens, C. D. M. Trang, L. J. Enman, J. Deng, S. W. Boettcher, *J. Am. Chem. Soc.* **2017**, *139*, 11361–11364.
- [119] D. Friebe, M. W. Louie, M. Bajdich, K. E. Sanwald, Y. Cai, A. M. Wise, M.-J. Cheng, D. Sokaras, T.-C. Weng, R. Alonso-Mori, R. C. Davis, J. R. Bargar, J. K. Nørskov, A. Nilsson, A. T. Bell, *J. Am. Chem. Soc.* **2015**, *137*, 1305–1313.
- [120] A. S. Batchellor, S. W. Boettcher, *ACS Catal.* **2015**, *5*, 6680–6689.
- [121] A. D. Doyle, M. Bajdich, A. Vojvodic, *Catal. Lett.* **2017**, *147*, 1533–1539.
- [122] C. G. Morales-Guio, L. Liardet, X. Hu, *J. Am. Chem. Soc.* **2016**, *138*, 8946–8957.
- [123] C. Roy, B. Sebok, S. B. Scott, E. M. Fiordaliso, J. E. Sørensen, A. Bodin, D. B. Trimarco, C. D. Damsgaard, P. C. K. Vesborg, O. Hansen, I. E. L. Stephens, J. Kibsgaard, I. Chorkendorff, *Nat. Catal.* **2018**, *1*, 820–829.
- [124] V. Colic, M. Pohl, D. Scieszka, A. S. Bandarenka, *Catal. Today* **2016**, *262*, 24–35.
- [125] J. Tymoczko, V. Colic, A. Ganassin, W. Schuhmann, A. S. Bandarenka, *Catal. Today* **2015**, *244*, 96–102.
- [126] D. Strmcnik, K. Kodama, D. van der Vliet, J. Greeley, V. R. Stamenkovic, N. M. Marković, *Nat. Chem.* **2009**, *1*, 466–472.
- [127] B. Garlyyev, S. Xue, M. D. Pohl, D. Reinisch, A. S. Bandarenka, *ACS Omega* **2018**, *3*, 15325–15331.
- [128] S. Xue, B. Garlyyev, S. Watzelle, Y. Liang, J. Fichtner, M. D. Pohl, A. S. Bandarenka, *ChemElectroChem* **2018**, *5*, 2326–2329.
- [129] B. Garlyyev, S. Xue, S. Watzelle, D. Scieszka, A. S. Bandarenka, *J. Phys. Chem. Lett.* **2018**, *9*, 1927–1930.
- [130] B. Garlyyev, Y. Liang, S. Xue, S. Watzelle, J. Fichtner, W. J. Li, X. Ding, A. S. Bandarenka, *Curr. Opin. Electrochem.* **2019**, *14*, 206–213.
- [131] S. Xue, B. Garlyyev, A. Auer, J. Kunze-Liebhäuser, A. S. Bandarenka, *J. Phys. Chem. C* **2020**, *124*, 12442–12447.
- [132] J. X. Wang, N. M. Marković, R. R. Adzic, *J. Phys. Chem. B* **2004**, *108*, 4127–4133.
- [133] F. Calle-Vallejo, J. Tymoczko, V. Colic, Q. H. Vu, M. D. Pohl, K. Morgenstern, D. Loffreda, P. Sautet, W. Schuhmann, A. S. Bandarenka, *Science* **2015**, *350*, 185–189.
- [134] Y. Liang, D. McLaughlin, C. Csoklich, O. Schneider, A. S. Bandarenka, *Energy Environ. Sci.* **2019**, *12*, 351–357.
- [135] J. Suntivich, E. E. Perry, H. A. Gasteiger, Y. Shao-Horn, *Electrocatalysis* **2013**, *4*, 49–55.
- [136] B. M. Hunter, W. Hieringer, J. R. Winkler, H. B. Gray, A. M. Müller-Hunter, *Energy Environ. Sci.* **2016**, *9*, 1734–1743.
- [137] J. D. Michael, E. L. Demeter, S. M. Illes, Q. Fan, J. R. Boes, J. R. Kitchin, *J. Phys. Chem. C* **2015**, *119*, 11475–11481.
- [138] J. Zaffran, M. B. Stevens, C. D. M. Trang, M. Nagli, M. Shehadeh, S. W. Boettcher, M. Caspary-Toroker, *Chem. Mater.* **2017**, *29*, 4761–4767.
- [139] C. Andronesco, S. Seisel, P. Wilde, S. Barwe, J. Masa, Y.-T. Chen, E. Ventosa, W. Schuhmann, *Chem. Eur. J.* **2018**, *24*, 13773–13777.
- [140] J. Kibsgaard, Z. Chen, B. N. Reinecke, T. F. Jaramillo, *Nat. Mater.* **2012**, *11*, 963–969.
- [141] H. Fei, J. Dong, D. Chen, T. Hu, X. Duan, I. Shakir, Y. Huang, X. Duan, *Chem. Soc. Rev.* **2019**, *48*, 5207–5241.
- [142] M. E. M. Buan, A. Cognigni, J. C. Walmsley, N. Muthuswamy, M. Rønning, *Catal. Today* **2020**, *357*, 248–258.
- [143] J. Timoshenko, B. R. Cuenya, *Chem. Rev.* **2020**, *121*, 882–961.
- [144] S. Mukerjee, S. Srinivasan, M. P. Soriaga, J. McBreen, *J. Electrochem. Soc.* **1995**, *142*, 1409–1422.
- [145] Y. Yang, Y. Wang, Y. Xiong, X. Huang, L. Shen, R. Huang, H. Wang, J. P. Pastore, S.-H. Yu, L. Xiao, J. D. Brock, L. Zhuang, H. D. Abruña, *J. Am. Chem. Soc.* **2019**, *141*, 1463–1466.
- [146] Y. Liang, H. Wang, J. Zhou, Y. Li, J. Wang, T. Regier, H. Dai, *J. Am. Chem. Soc.* **2012**, *134*, 3517–3523.
- [147] N. Ebejer, M. Schnippering, A. W. Colburn, M. A. Edwards, P. R. Unwin, *Anal. Chem.* **2010**, *82*, 9141–9145.
- [148] M. E. Snowden, A. G. Güell, S. C. S. Lai, K. McKelvey, N. Ebejer, M. A. O'Connell, A. W. Colburn, P. R. Unwin, *Anal. Chem.* **2012**, *84*, 2483–2491.
- [149] N. Ebejer, A. G. Güell, S. C. S. Lai, K. McKelvey, M. E. Snowden, P. R. Unwin, *Annu. Rev. Anal. Chem.* **2013**, *6*, 329–351.
- [150] A. G. Güell, K. E. Meadows, P. V. Dudin, N. Ebejer, J. V. Macpherson, P. R. Unwin, *Nano Lett.* **2013**, *14*, 220–224.
- [151] P. R. Unwin, A. G. Güell, G. Zhang, *Acc. Chem. Res.* **2016**, *49*, 2041–2048.
- [152] J. C. Byers, A. G. Güell, P. R. Unwin, *J. Am. Chem. Soc.* **2014**, *136*, 11252–11255.
- [153] T. Tarnev, H. B. Aiyappa, A. Botz, T. Erichsen, A. Ernst, C. Andronesco, W. Schuhmann, *Angew. Chem. Int. Ed.* **2019**, *58*, 14265–14269; *Angew. Chem.* **2019**, *131*, 14403–14407.
- [154] J. H. K. Pfisterer, Y. Liang, O. Schneider, A. S. Bandarenka, *Nature* **2017**, *549*, 74–77.
- [155] Y. Liang, C. Csoklich, D. McLaughlin, O. Schneider, A. S. Bandarenka, *ACS Appl. Mater. Interfaces* **2019**, *11*, 12476–12480.

- [156] E. Mitterreiter, Y. Liang, M. Golibrzuch, D. McLaughlin, C. Csoklich, J. D. Bartl, A. Holleitner, U. Wurstbauer, A. S. Bandarenka, *NPJ 2D Mater. Appl.* **2019**, *3*, 25.
- [157] R. M. Kluge, R. W. Haid, A. S. Bandarenka, *J. Catal.* **2021**, *396*, 14–22.
- [158] R. M. Kluge, R. W. Haid, I. E. L. Stephens, F. Calle-Vallejo, A. S. Bandarenka, *Phys. Chem. Chem. Phys.* **2021**, *23*, 10051–10058.
- [159] J. Halbritter, G. Repphun, S. Vinzelberg, G. Staikov, W. J. Lorenz, *Electrochim. Acta* **1995**, *40*, 1385–1394.
- [160] M. Hugelmann, W. Schindler, *Surf. Sci.* **2003**, *541*, L643–L648.
- [161] M. Hugelmann, W. Schindler, *J. Electrochem. Soc.* **2004**, *151*, E97–E101.
- [162] F. C. Simeone, D. M. Kolb, S. Venkatachalam, T. Jacob, *Angew. Chem. Int. Ed.* **2007**, *46*, 8903–8906; *Angew. Chem.* **2007**, *119*, 9061–9064.
- [163] X. Chen, A. Maljus, R. A. Rincón, A. Battistel, A. S. Bandarenka, W. Schuhmann, *Chem. Commun.* **2014**, *50*, 13250–13253.
- [164] J. H. K. Pfisterer, M. Baghernejad, G. Giuzio, K. F. Domke, *Nat. Commun.* **2019**, *10*, 5702.
- [165] R. R. Rao, M. J. Kolb, N. B. Halck, A. F. Pedersen, A. Mehta, H. You, K. A. Stoerzinger, Z. Feng, H. A. Hansen, H. Zhou, L. Giordano, J. Rossmeis, T. Vegge, I. Chorkendorff, I. E. L. Stephens, Y. Shao-Horn, *Energy Environ. Sci.* **2017**, *10*, 2626–2637.

Manuscript received: April 30, 2021

Revised manuscript received: July 8, 2021

Accepted manuscript online: July 8, 2021